

# 1 Future changes in seasonal climate predictability

2

3 Dillon J. Amaya<sup>1</sup>, Nicola Maher<sup>2,3,4</sup>, Clara Deser<sup>5</sup>, Michael G. Jacox<sup>1,6</sup>, Michael A. Alexander<sup>1</sup>,  
4 Matthew Newman<sup>1</sup>, Juliana Dias<sup>1</sup>, and Jiale Lou<sup>7</sup>

5

6 <sup>1</sup>Physical Science Laboratory, National Oceanic and Atmospheric Administration, 325  
7 Broadway, Boulder, CO 80305, USA

8 <sup>2</sup>Cooperative Institute for Research in Environmental Sciences, University of Colorado  
9 Boulder, 216 UCB, University of Colorado Boulder campus, Boulder, CO 80309, USA

10 <sup>3</sup>Department of Atmospheric and Oceanic Sciences (ATOC), University of Colorado at  
11 Boulder, Boulder, CO 80309, USA

12 <sup>4</sup>Australian National University, Canberra, ACT 0200, Australia

13 <sup>5</sup>National Science Foundation National Center for Atmospheric Research, 1850 Table Mesa  
14 Dr, Boulder, CO 80305, USA

15 <sup>6</sup>Environmental Research Division, Southwest Fisheries Science Center, National Oceanic  
16 and Atmospheric Administration, 99 Pacific St #255A, Monterey, CA 93940, USA

17 <sup>7</sup>Atmospheric and Oceanic Sciences Program, Princeton University, Princeton, NJ, USA

18

19

20

21

22

23 Corresponding author: Dillon J. Amaya, [dillon.amaya@noaa.gov](mailto:dillon.amaya@noaa.gov), 816-916-8348

24

25 **Abstract**

26 Seasonal forecasts provide critical decision support tools for managing important  
27 socioeconomically-relevant resources. As the result of continued model development, the skill of  
28 such tools has improved over the years. However, further advancements are hampered by the  
29 climate’s “potential predictability”, a potential upper limit for how accurately we can predict  
30 different climate states. Recent studies have shown that potential predictability and actual forecast  
31 skill have varied throughout the historical record, primarily as a result of natural decadal  
32 variability. In this study, we explore whether potential predictability will change in the future as a  
33 distinct response to anthropogenic climate change. We estimate the potential predictability limits  
34 of the El Niño-Southern Oscillation (ENSO) as well as global surface temperature, precipitation,  
35 and upper atmospheric circulation anomalies from 1921-2100 within a perfect model framework.  
36 Simulated potential predictability changes by 2100 vary across five different coupled model large  
37 ensembles: depending upon the model, we find a robust increase, robust decrease, or no significant  
38 change in predictability. Yet, despite this large inter-model uncertainty, we find that predictability  
39 changes across the models are strongly linked to their projected change in ENSO amplitude, with  
40 a 10% change in Nino3.4 standard deviation giving rise to a 14% change in globally averaged  
41 forecast skill at 12-month lead. This common physical relationship suggests that changes in global  
42 potential predictability in the coming decades will be linked to anthropogenic climate change of  
43 ENSO. As a result, historical forecast skill relationships that depend on ENSO and its  
44 teleconnections may be altered as the climate continues to change.

45

## 46 **1. Introduction**

47           Seasonal climate forecasts provide important decision support tools to help stakeholders  
48 manage a variety of socioeconomically-relevant resources. For example, initialized dynamical  
49 forecasts are routinely used to provide seasonal outlooks of regional precipitation and surface  
50 temperature, tropical cyclone activity, and climate modes such as the El Niño-Southern Oscillation  
51 (ENSO). While recent advances in model physics, resolution, ensemble sizes, and data  
52 assimilation schemes have led to increases in seasonal forecast skill (Barnston et al. 2012; Barnston  
53 and Tippett 2017), prediction systems may still be limited by the so-called “potential  
54 predictability” of different climate states. Potential predictability is often thought of as a prediction  
55 limit intrinsic to the chaotic nature of the climate system (Sardeshmukh et al. 2000), the point when  
56 a forecast’s initial uncertainty grows until any climate state randomly drawn from the  
57 climatological probability distribution could be expected to occur (Lorenz 1969). In practice,  
58 however, predictability is generally estimated from models, but model predictability may differ  
59 from nature’s predictability due to model errors both in the distribution of climate states and their  
60 evolution. Systematic state-dependent seasonal forecast errors (e.g., Beverley et al. 2023) likewise  
61 suggest that some aspects of nature's predictability may be missed by all model predictability  
62 studies. Recent studies have even suggested that some models make forecasts in some regions with  
63 real-world skill that exceeds the model’s own predictability, possibly a consequence of the signal-  
64 to-noise paradox (e.g., Scaife and Smith 2018; Weisheimer et al. 2024). However, regardless of  
65 whether estimates of a model’s potential predictability represent a “hard” or a “soft” ceiling to its  
66 forecast skill, its presence suggests that further reduction of model biases may yield only  
67 incremental increases in forecast skill as these limits are reached (or slightly exceeded) for different  
68 aspects of the climate system (e.g., Newman & Sardeshmukh, 2017).

69           Recent studies have shown that potential predictability is not stationary or fixed in time  
70 (Newman & Sardeshmukh, 2017; Weisheimer et al., 2022; Zhao et al., 2016). As a result, actual  
71 forecast skill has also varied substantially in the past (Derome et al., 2005; Kumar, 2009; MacLeod  
72 et al., 2018; O’Reilly et al., 2017, 2019; Shi et al., 2015; Weisheimer et al., 2017, 2019), although  
73 overall secular trends in this skill may be harder to detect in the historical record (Ding et al. 2019).  
74 For example, Lou et al. (2023) and Weisheimer et al. (2022) showed that long-lead ENSO forecast  
75 skill was higher at the beginning and end of the twentieth century, with a multidecadal period of  
76 lower skill from the 1930s-1950s. Further, Weisheimer et al. (2020) found that past seasonal

77 predictability of extratropical atmospheric circulation patterns such as the Pacific-North American  
78 (PNA) pattern and the North Atlantic Oscillation (NAO) have also experienced pronounced  
79 decadal variations. While these past changes in prediction skill may result from varied model  
80 performance relative to historical observations (e.g., Weisheimer et al., 2022), these skill changes  
81 may also be driven by changes in the intrinsic predictability of the climate system itself (Becker et  
82 al. 2014; Newman and Sardeshmukh 2017).

83         Given these historical changes, it is reasonable to expect that potential predictability and  
84 actual prediction skill may similarly vary in the future, whether as a result of natural decadal  
85 variability (Weisheimer et al., 2020), a possible response to anthropogenic climate change (Zheng  
86 et al. 2022), or some combination of both. In particular, some general circulation models (GCMs)  
87 project that ENSO and its remote impacts may change in response to an increase in greenhouse  
88 gasses (e.g., Cai et al., 2021). For example, some models project significant changes in ENSO  
89 variability (Maher et al. 2023; Heede and Fedorov 2023), frequency (Berner et al. 2020), flavor  
90 (i.e., central vs eastern Pacific; Capotondi et al., 2015), and teleconnection strength/position (Gan  
91 et al. 2017; McGregor et al. 2022; O’Brien and Deser 2023; Zhou et al. 2014), although there is  
92 substantial uncertainty in the sign and intensity of these changes across models. Still, through its  
93 far-reaching teleconnections, ENSO is the single most important source of predictability on  
94 seasonal timescales for much of the globe (e.g., Barnett & Preisendorfer, 1987; Jacox et al., 2019;  
95 Quan et al., 2006), suggesting that any future changes to ENSO’s strength and/or its connectivity  
96 to the rest of the climate system could significantly impact the potential predictability of many  
97 socioeconomically-relevant climate parameters.

98         It is crucial to assess how potential predictability may evolve as climate continues to  
99 change. Many previous studies have used hindcast systems to estimate potential predictability in  
100 the past (e.g., Shi et al., 2015; Weisheimer et al., 2019, 2020, 2022). However, model hindcasts  
101 are not useful for quantifying possible future changes in predictability as they are by definition  
102 retrospective and depend on past observations for their initialization. A different technique that  
103 can overcome these limitations and assess time-varying climate predictability in the past and the  
104 future is the “model-analog” approach. In the traditional analog framework, past observed climate  
105 states are found that closely match the current state and their subsequent evolution are treated as  
106 forecasts (Lorenz 1969). Alternatively, coupled GCMs allow for analogs to be drawn from climate  
107 simulations (often pre-industrial control runs; Ding et al., 2018), with the model evolution of these

108 analogs then treated as the forecast. This method increases the “library” of possible climate states  
109 to compare against the current observed state, resulting in closer analog matches and allowing for  
110 the generation of forecast ensembles. Such model-analog forecasts have been shown to be as  
111 skillful as initialized dynamical forecasts (Ding et al. 2018, 2019), with the added benefit of being  
112 more computationally efficient.

113 The “perfect model-analog” technique utilizes these same methods, but whereas the goal  
114 of a traditional model-analog is to leverage climate simulations to forecast the real world, the goal  
115 of the perfect model framework is to instead forecast the climate simulation itself. This is  
116 accomplished by treating a portion of a climate simulation as “observations”, and then drawing  
117 the analog forecasts from a different, independent portion of the same climate simulation. The  
118 resulting ensemble forecast is “perfect” in that it has no unconditional or conditional biases (von  
119 Storch & Zwiers, 1999). Thus, the forecast skill in a perfect model framework is a measure of the  
120 potential predictability (or equivalently, “potential skill”) in the climate system. Since the perfect  
121 model framework does not depend on real-world observations, it can be readily applied to past and  
122 future climate simulations to explore how these predictability limits change over time.

123 In this study, we estimate how seasonal climate predictability varies from 1921-2100 by  
124 applying the perfect model framework to five coupled model initial condition large ensembles  
125 (LEs) that are each forced with time-varying radiative forcing. Model LEs have been widely used  
126 in climate science studies to separate the response to external forcing from internal climate  
127 variations (see review by Maher et al., 2021). In our analysis, the large number of ensemble  
128 members provided by each model LE (ranging from 30-100 depending on model) allows us to  
129 generate hundreds of thousands of perfect model forecasts with which to assess any future changes  
130 in potential predictability. In particular, we generate 24-month forecasts of global surface  
131 temperature, precipitation, and upper atmospheric circulation anomalies as well as for ENSO. The  
132 forecasts are then verified against independent portions of the same large ensembles using anomaly  
133 correlation coefficient (ACC). We then relate future changes in potential predictability to future  
134 ENSO changes in each model. Finally, we assess how well the model LEs predict the real world.

135

## 136 **2. Data and Methods**

137 *(a) Climate model large ensemble simulations and observations*

138 We apply the perfect model framework to five coupled model initial condition LEs that  
139 span the Coupled Model Intercomparison Project Phase 5 (CMIP5) and CMIP6 eras (Table 1).  
140 Such a comparison across models allows us to test the sensitivity of our results to inter-model  
141 uncertainty found in the climate response to increased radiative forcing. For efficiency, all model  
142 data output was first interpolated to a common  $2.5^\circ \times 2.5^\circ$  grid.

143 The models used in our analysis include: the Community Earth System Model version 1.2  
144 LE (CESM1-LE; 40 members; (Kay et al. 2015), CESM version 2 LE (CESM2-LE; 100 members;  
145 Rodgers et al., 2021), the Geophysical Fluid Dynamics Laboratory Seamless System for Prediction  
146 and Earth System Research Medium Resolution Simulation (GFDL-SPEAR; 30 members;  
147 Delworth et al., 2020), the GFDL Earth System Modeling version 2M (GFDL-ESM2M; 30  
148 members; Burger et al. 2020, 2022), and the Max-Planck Institute Grand Ensemble (MPI-GE; 100  
149 members; Maher et al., 2019). The analysis period is 1921-2100, during which each model uses a  
150 specified external forcing scenario: (1) historical + representative concentration pathway 8.5  
151 (RCP8.5), (2) historical + shared socioeconomic pathway 3-7.0 (SSP3-7.0), or (3) historical +  
152 SSP5-8.5. Within a given model, each ensemble member starts from a different initial condition.  
153 Over time, the ensemble members diverge due to the chaotic nature of the coupled climate system.  
154 As a result, once the memory of the initial condition fades, each ensemble member can be treated  
155 as an independent sample of the climate that has its own unique sequence of internal variability  
156 superimposed on a common forced response. We compare a portion of our model results to  
157 monthly mean data from four different observational sea surface temperature (SST) datasets: the  
158 National Oceanic and Atmospheric Administration (NOAA) Extended Reconstructed Sea Surface  
159 Temperature version 5 (ERSSTv5; Huang et al., 2017), Hadley Centre Sea Ice and Sea Surface  
160 Temperature (HadISST; Rayner et al. 2003), Centennial in situ Observation-Based Estimates  
161 versions 1 (COBE; Ishii et al. 2005) and 2 (COBE2; Hirahara et al. 2014). We primarily compare  
162 these observational products during the period 1921-2023. Differences in data streams and gap  
163 filling methods lead to differences between each observational estimate during the early part of  
164 the 20<sup>th</sup> century. However, the observations are in better agreement during a more recent period  
165 (e.g., 1980-2023).

166  
167

Dataset	Forcing (ens. size)	$\sigma_{3.4}$ trend ( $^{\circ}\text{C dec}^{-1}$ )	$\sigma_{3.4}$ trend ( $^{\circ}\text{C dec}^{-1}$ )	Reference
		1950-2023	1950-2100	
CESM1-LE	HIST+RCP8.5 (40)	$0.04 \pm 0.03$	$0.02 \pm 0.02$	Kay et al. (2015)
CESM2-LE	HIST+SSP3-7.0 (100)	$0.03 \pm 0.04$	$0.00 \pm 0.02$	Rodgers et al. (2021)
GFDL-SPEAR	HIST+SSP5-8.5 (30)	$0.02 \pm 0.03$	$0.03 \pm 0.01$	Delworth et al. (2020)
GFDL-ESM2M	HIST+RCP8.5 (30)	$0.02 \pm 0.05$	$-0.02 \pm 0.02$	Burger et al. (2020), (2022)
MPI-GE	HIST+RCP8.5 (100)	$0.00 \pm 0.04$	$0.00 \pm 0.01$	Maher et al. (2019)
ERSSTv5		0.03		Huang et al. (2017)
HadISST		0.07		Rayner et al. (2003)
COBE		0.07		Ishii et al. (2005)
COBE2		0.06		Hirahara et al. (2014)

168 **Table 1** Observational and model datasets used in this study. First column: radiation forcing scenario used by  
169 each model. The number of ensemble members available in each model is in parentheses. Second column:  
170 December-February averaged Nino3.4 standard deviation ( $\sigma_{3.4}$ ) trend ( $^{\circ}\text{C decade}^{-1}$ ) in 30-year running windows  
171 (i.e., Figure 1) for the period 1921-2023. For climate models, the ensemble mean trend is reported along with  
172 +/- one standard deviation. Third column: As in the second column, but for the period 1921-2100. Fourth column:  
173 Dataset references.  
174

175 *(b) Perfect model-analog framework*

176 In each LE, perfect model forecasts are generated and evaluated for different 30-year  
177 periods spaced every 10 years from 1921-2100 (e.g., 1921-1950, 1931-1960...2071-2100). The  
178 forecasts are produced within each of these 30-year periods separately using the following method.

179 For a given model and 30-year period:

- 180 (1) We extract monthly mean SSTs from each ensemble member for the 30-year period of  
181 interest.
- 182 (2) We then remove the long-term monthly mean SSTs at each grid point based on the  
183 contemporaneous climatology calculated using all ensemble members (i.e., anomalies  
184 in 1921-1950 are relative to a 1921-1950 climatology).
- 185 (3) We further remove the ensemble mean SST anomaly (SSTA) (i.e., the model-specific  
186 externally-forced signal) at each grid point from each of the model's individual  
187 ensemble members.

- 188 (4) We arbitrarily treat the 1<sup>st</sup> ensemble member as the “truth” or “observations”. Because  
189 each ensemble member is independent from one another, a data library of possible  
190 analog matches to the “observations” can then be constructed for each calendar month  
191 using the remaining ensemble members. For example, the data library for January in  
192 CESM1-LE consists of 39 ensemble members x 28 years = 1092 samples. Note that it  
193 is only 28 years because we aim to generate 24-month forecasts, so any possible analog  
194 matches in the final two years would extend beyond our 30-year window of interest.  
195 Thus, the final two years in each 30-year window are excluded from our data libraries.
- 196 (5) For a given month, we choose analogs by minimizing the distance between the climate  
197 state in the “observed” ensemble member and those found in the corresponding  
198 monthly data library (i.e., by comparing an “observed” January to the January data  
199 library). The distance between climate states is estimated by calculating the total root-  
200 mean-squared (RMS) difference between the “observed” SSTAs from 60°S-60°N and  
201 at all longitudes and those from every possible match in the data library. Note that we  
202 do not area weight the RMS difference calculation used in our analysis (see following  
203 section for more details). The distances are then ranked in descending order. The 10  
204 closest states from the data library and their subsequent 24-month evolution are chosen  
205 as the forecast ensemble for that month.
- 206 (6) We repeat (4)-(5) by treating each other model ensemble member as “observations”  
207 and constructing the monthly data library using the remaining ensemble members.

208 This procedure generates a 10-member forecast for every month and every ensemble  
209 member in a given model LE. For example, applying this perfect model framework to CESM1-LE  
210 for a given 30-year period generates 40 (ensemble members) x 12 (calendar months) x 28 (years)  
211 = 13,400 10-member, 24-month forecasts with which we can estimate seasonal climate  
212 predictability. Although we use SSTAs to identify analogs, we are not limited only to SSTA  
213 forecasts for analysis. Once the nearest climate states are selected, the evolution of any model  
214 variable can be treated as a forecast and subsequently verified against the corresponding variable  
215 from “observations” (e.g., Ding et al., 2019). In this way, we assess the forecast anomalies of the  
216 following monthly mean variables from each model, with the CMIP standard variable name shown  
217 in parenthesis: SST (tos), 2m air temperature over land (tas), precipitation (pr), and the 500mb  
218 streamfunction, which was calculated using the U/V wind components at 500mb (ua, va). As



219 previously mentioned for SST, anomalies for all other variables are derived by removing both the  
220 long-term monthly means of the contemporaneous 30-year period and each model’s respective  
221 ensemble mean.

222

223 *(c) Perfect model-analog sensitivities*

224 There are several arbitrary choices that must be made when adapting the perfect model-  
225 analog technique for LEs. Here, we briefly discuss these decisions and how they might influence  
226 our results or conclusions. (1) We remove a given model’s ensemble mean from each of its  
227 members in order to isolate the internal component of each parameter, while still allowing for the  
228 rectification of the forced response on climate variability. Doing so allows us to focus on possible  
229 forced changes in the predictability of climate variations, as opposed to the more trivial exercise  
230 of predicting the forced trend. (2) Ding et al. (2018) showed that for data libraries of several  
231 hundreds of years, analog forecast ensembles of 10-20 members produced the most accurate  
232 forecasts. This is because larger forecast ensembles include increasingly poor analog matches,  
233 resulting in lower skill over the length of the forecast. We choose the top 10 analogs for our  
234 forecast ensembles for computational efficiency; however, our results and conclusions are not  
235 qualitatively impacted when increasing the forecast ensemble size to the top 15 or 20 matches. (3)  
236 We do not area weight the RMS difference calculation so as not to overweight the tropics when  
237 drawing analogs. We find that this choice increases the overall forecast skill in the mid-latitudes  
238 without overly decreasing it in the tropics. We select analogs based on SSTAs from 60°S-60°N  
239 and at all longitudes for similar reasons (i.e., to improve the representation of the extratropics when  
240 selecting analogs). Our results and conclusions are not qualitatively impacted by these decisions.

241

242 *(d) Potential predictability metrics and signal-to-noise*

243 To assess lead-dependent potential skill in each model, we calculate  $N_e$  estimates of the  
244 anomaly correlation coefficient (ACC) between each ensemble mean forecast and the  
245 corresponding “observations”, where  $N_e$  is the number of ensemble members in a given LE (i.e.,  
246 the number of “observed” timeseries used to generate analogs). For example, there are 40 estimates  
247 of the ACC for 1921-1950 when evaluating CESM1-LE. We repeat this procedure for each 30-  
248 year period separately, and we report the ensemble mean ACC in our results. We test the  
249 significance of the ensemble mean ACC using a 95% confidence interval based on two-sample  $t$ -

250 test. We further determine the robustness of the change in ACC between 30-year periods by  
 251 indicating where 80% of a given model's ensemble members agree on the sign of the change. Note  
 252 that all of our results are consistent with each other when using probabilistic skill metrics (e.g.,  
 253 Brier Skill Score or reliability). However, for brevity, we only show skill based on ACC.

254 We assess the lead-dependent signal-to-noise (S2N) ratio in our forecasts following  
 255 Sardeshmukh et al. (2000). For each model ensemble member  $N_e$ , the S2N ratio at lead  $l$  is:

$$256 \quad S2N(N_e, l) = \left( \frac{\sum_{i=1}^n \bar{x}_f'^2}{\frac{1}{K} \sum_{i=1}^m x_f'^2} \right)^{1/2} \quad (1)$$

257 Where  $x_f' = x_f - \bar{x}_f$  is the deviation of each individual forecast member ( $x_f$ ) from the ensemble  
 258 mean forecast ( $\bar{x}_f$ ) for each monthly initialization ( $i$ ). The numerator in Eq. (1) represents the  
 259 signal, and is calculated as the square of  $\bar{x}_f$  summed over all monthly initializations in a given 30-  
 260 year period ( $n$ ). The denominator represents the noise, and is calculated as the square of  $x_f'$   
 261 summed over  $m$ , where  $m$  is the total number of monthly initializations from all forecast ensemble  
 262 members  $K$  (in our analysis  $K = 10$ ). Therefore, for a given 30-year period,  $n = 12$  (calendar  
 263 months) x 28 (years) = 336 and  $m = 3360$ . As with ACC, we calculate  $N_e$  estimates of the S2N  
 264 ratio for each LE (one for each ensemble member), and report the ensemble mean values in our  
 265 results. A higher S2N ratio indicates that there is a larger ensemble mean anomaly and/or less  
 266 spread among the forecast ensemble, which results in a more skillful forecast in the perfect model  
 267 framework (Sardeshmukh et al. 2000).

268 Future changes in ACC and S2N are shown relative to a reference period of 1921-1950.  
 269 This reference was chosen as it is the earliest common period among the model LEs and because  
 270 it allows us to quantify the largest possible radiatively forced change in each model. Note that  
 271 while CESM2-LE, GFDL-ESM2M, and MPI-GE were initialized in the mid-19<sup>th</sup> century, CESM1-  
 272 LE and GFDL-SPEAR were initialized in 1920 and 1921, respectively. Since the ensemble  
 273 members in GFDL-SPEAR were initialized from different years of a pre-industrial control  
 274 simulation with different ocean states, they are already well separated. However, since the  
 275 ensemble members in CESM1-LE were initialized with a similar ocean state, it is possible that the  
 276 ocean memory of the initial condition is present in this model for the earliest 30-year period over  
 277 which we quantify predictability (i.e., 1921-1950). However, we have repeated our analysis using  
 278 1991-2020 as the reference period and found that our results and conclusions are not qualitatively  
 279 impacted by this choice.

280

281 *(e) Observed model-analogs and dynamical forecasts*

282 In Section 3d, we compare model-analog forecasts of observed SSTA to seasonal SSTA  
283 forecasts obtained from six global climate models contributing to the North American Multimodel  
284 Ensemble (NMME; Kirtman et al. 2014; Becker et al. 2022). Each of the NMME models consist  
285 of an ensemble of forecasts that are initialized each month (see Table S1 for model details). We  
286 calculate forecast skill in NMME based on a set of reforecasts (also known as retrospective  
287 forecasts or hindcasts) available for each model. Reforecasts are forecasts of past periods, using  
288 information that was only available at the time of forecast initialization. The historical skill derived  
289 from these reforecasts provides an important evaluation of the skill inherent to each forecast  
290 system. The SSTAs from each NMME model are relative to a lead-dependent climatology from  
291 1991-2020. Before calculating skill, the lead-dependent linear trend is also removed from all  
292 NMME SSTA forecasts.

293 We produce observed model-analog forecasts from each LE following the methods  
294 outlined in Section 2b, except analog forecasts are drawn by matching observed SSTA from  
295 ERSSTv5 for every month from 1991-2020. Additionally, for each model LE, the data library that  
296 model-analog forecasts are drawn from includes all ensemble members (i.e., none are left out as  
297 the “truth” is taken to be ERSSTv5). For example, the data libraries in CESM1-LE consist of 40  
298 ensemble members x 30 years = 1200 samples for each calendar month. The result is a 10-member  
299 model-analog reforecast for each of the five model LEs. Forecast skill for both NMME and the  
300 observed model-analogs is then evaluated by comparing to ERSSTv5 from 1991-2020. This period  
301 was chosen as it is the longest overlapping record available for the NMME models.

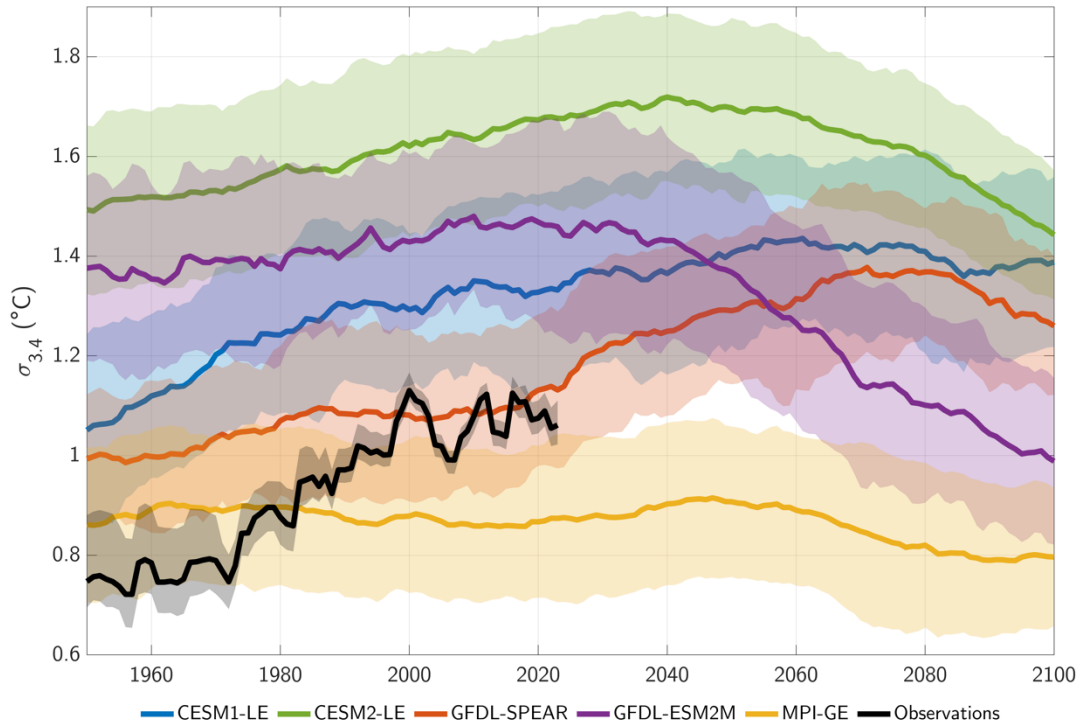
302

303 **3. Results**

304 *(a) Forced changes in ENSO amplitude*

305 Given ENSO’s dominant role in driving seasonal climate predictability, we first assess the  
306 simulated response of ENSO amplitude to historical and future radiative forcing in each LE. The  
307 CESM1-LE shows a consistent increase in Nino3.4 (i.e., SSTA averaged 5°S-5°N, 170°W-120°W)  
308 standard deviation from 1921-2060, after which it levels off (Figure 1 and Table 1). The Nino3.4  
309 amplitude in GFDL-SPEAR is relatively stable from 1921-2020, after which it increases until  
310 about 2080 before decreasing slightly. In contrast, the ENSO variability in CESM2-LE rises

311 consistently through 2040 before decreasing consistently through 2100. In GFDL-ESM2M,  
 312 Nino3.4 standard deviation is relatively stable until about 2040, after which it sharply decreases  
 313 through the end of the century. In MPI-GE, there is little change in Nino3.4 variability throughout  
 314 the record. The large inter-model uncertainty in future ENSO variability is consistent with Maher  
 315 et al. (2023, see their Figure 4).  
 316



317  
 318 **Figure 1** Standard deviation of December-February averaged SSTA in the Nino3.4 region in running 30-year  
 319 windows from 1921-2100. Years indicate end of the window (e.g., 1960=1931-1960). Colors represent different  
 320 model large ensembles, with thick curves for ensemble mean values and shading for one standard deviation  
 321 spread across the ensemble. Black shading shows the range of observed values from 1921-2023 from four  
 322 different observational products (ERSSTv5, HadISST, COBE, and COBE2), with the black curve representing  
 323 the observed average. See Figure S1 for individual observational estimates.  
 324

325 With the exception of MPI-GE in the early 20<sup>th</sup>-century and GFDL-SPEAR in the later  
 326 20<sup>th</sup>-century, each model LE exhibits positive variability biases relative to observations (Figure 1  
 327 black line). Given these biases and other known climate model errors concerning observed trends  
 328 in the tropical Pacific (Wills et al. 2022), it is reasonable to wonder whether these LEs are reliable  
 329 tools for diagnosing future changes in climate variability or, by extension, predictability. Despite  
 330 the variability biases, however, we find that the simulated historical change in Nino3.4 amplitude  
 331 is well within each model’s ensemble spread (Table 1 and Figures S1-S2), suggesting that the

332 forced response in Nino3.4 amplitude as simulated by any of these climate models could plausibly  
333 exist in observations given the correct combination of internal variability. As a result, the projected  
334 changes from one (biased) climate state to another (biased) climate state in these LEs can inform  
335 our real-world expectations of the future, with the largest source of uncertainty coming from the  
336 different modeled forced responses. Based on these results, we primarily focus on CESM1-LE,  
337 MPI-GE, and GFDL-ESM2M when evaluating the forecast skill of our perfect model-analogs as  
338 these LEs span the range of possible changes in future ENSO amplitude (i.e., increasing, no  
339 change, and decreasing, respectively).

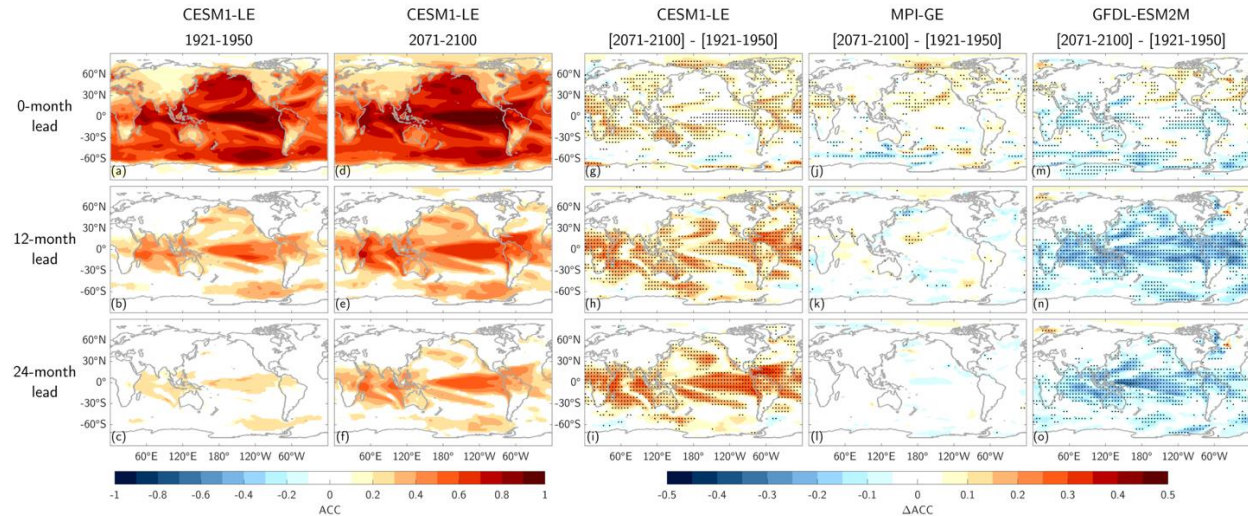
340

341 *(b) Potential predictability and future changes*

### 342 **1) Sea surface temperature and surface air temperature**

343 Perfect model-analog forecasts (hereafter referred to as “forecasts”) of SSTA for 1921-  
344 1950 in CESM1-LE show significant potential skill (hereafter referred to as “skill”) at 0-month  
345 lead (i.e., the “initialization” or the month that was used to determine the analogs) for most of the  
346 globe (globally averaged ACC = 0.62), with the tropical Pacific exhibiting the highest skill (ACCs  
347 > 0.9; Figure 2a). There is also significant skill of surface air temperature anomalies over land  
348 (SATA) at 0-month lead in most regions. However, SATA skill is generally weaker than for SSTA  
349 (global average ACC = 0.48), especially in mid-latitudes. The higher overall SSTA skill or  
350 “potential predictability” (hereafter referred to as “predictability”) at 0-month lead is expected  
351 since our analogs are chosen by minimizing the distance between the “observed” SSTA and the  
352 data library. Indeed, the high 0-month lead SSTA skill gives us confidence that the perfect model  
353 framework is reliably drawing analogs that closely correspond to the “observed” climate states at  
354 each initialization. Results are similar for the other LEs (Figures S3-S7).

355



356

357 **Figure 2** Surface temperature potential predictability. (a)-(c) Ensemble mean skill of surface temperature  
 358 anomalies in CESM1-LE as measured by ACC calculated across all months in the period 1921-1950. (d)-(f) As  
 359 in (a)-(c), but for the period 2071-2100. (g)-(o) Change in ACC between past and future periods for (g)-(i)  
 360 CESM1-LE (j)-(l) MPI-GE (m)-(o) GFDL-ESM2M. Skill values in (a)-(f) are only shown when 95% significant.  
 361 Stipples in (g)-(o) indicate where 80% of a respective model's ensemble agrees on the sign of the change. See  
 362 Figures S3-S7 for the full surface temperature anomaly skill in the other large ensembles.  
 363

364 We further assess the predictability at increasing lead times; however, for brevity, we only  
 365 show the skill at 12-month and 24-month leads (Figure 2b-c; see Figures S3-S7 for skill maps at  
 366 additional lead times). Skill of surface temperature decreases with increasing lead time, although  
 367 this reduction is more apparent for SATA than for SSTA. This difference is consistent with the  
 368 higher thermal capacity of the ocean relative to the atmosphere, which typically leads to higher  
 369 predictability at longer leads for SSTA than for SATA. In particular, SSTA ACCs at 12-month  
 370 lead exceed 0.6 in the tropical Pacific, consistent with previous model-analog forecast studies (e.g.,  
 371 Ding et al., 2018). There is also significant SATA predictability over tropical land surfaces, as well  
 372 as significant SSTA predictability throughout most of the North Pacific, the tropical Atlantic, the  
 373 tropical Indian Ocean, and the Southern Ocean west of the Drake Passage. These regions are  
 374 known to be influenced by large-scale ENSO teleconnections (e.g., He et al., 2020; Horel &  
 375 Wallace, 1981; Mo & Ghil, 1987), suggesting that ENSO is a key source of long-lead predictability  
 376 in our forecasts. Skill further degrades out to 24-month leads (Figure 2c); however, there is still  
 377 the significant SATA skill over northern South America and significant SSTA skill in the tropical  
 378 and South Pacific and the Indian Ocean.

379 In CESM1-LE, there is a robust increase in SSTA and SATA predictability in the future at  
 380 all leads, with only a few small regions of decreasing predictability (Figure 2d-i). In particular, the

381 0-month lead SSTA skill increases in the western tropical Pacific as well as the Indian and Atlantic  
382 Oceans (Figure 2i). Similarly, there is a robust increase in future SATA predictability at 0-month  
383 lead over much of Africa, portions of eastern Asia, equatorial South America, and all of Australia.  
384 An increase in forecast skill at 0-month lead implies that the distance between the “observed” and  
385 analog climate states decreases in the future (i.e., the analogs more closely match the  
386 “observations”). Further, the widespread ensemble agreement (black stipples) indicates that these  
387 predictability changes are a “robust” (defined here as 80% ensemble agreement on the sign of the  
388 change) part of the model’s forced response and not due to chance.

389 The CESM1-LE changes in SSTA/SATA predictability are starker at 12- and 24-month leads  
390 (Figure 2h-i), with robust increases in ACC throughout the global tropics in an ENSO-like pattern.  
391 The increased predictability along the equatorial Pacific, in particular, suggests that ENSO itself  
392 is more predictable in the future in CESM1-LE. We will explore ENSO predictability in more  
393 detail in Section 3d. There are also robust long-lead increases in SSTA and SATA predictability  
394 in the mid-latitudes. For example, there is an increase in SSTA skill in the North Atlantic in a  
395 pattern reminiscent of the SSTA footprint generated by the NAO (i.e., a horseshoe shape from  
396 southern Greenland to the tropical North Atlantic; Kushnir et al., 2006). There are also pronounced  
397 increases in SSTA skill in the North Pacific and along the U.S. west coast and SATA skill in the  
398 American Southwest, which may be associated with an eastward shift in ENSO’s teleconnections  
399 to the Pacific North America region (O’Brien and Deser 2023). Other LEs generally disagree with  
400 CESM1-LE on the sign and magnitude of future predictability changes (Figure 2j-o and Figures  
401 S3-S7). The MPI-GE at 0-month lead shows some isolated regions of increasing and decreasing  
402 SSTA/SATA skill, but without a clear pattern. At longer leads, the skill change in MPI-GE is close  
403 to zero nearly everywhere and there is little agreement among the ensemble on the sign of the  
404 change. In contrast, GFDL-ESM2M shows a robust decrease in SSTA/SATA predictability for  
405 most the globe (Figure 2m-o) in a similar ENSO-like pattern as seen in CESM1-LE (pattern  
406 correlation = -0.68 at 12-month lead), though with less loading in the Northeast Atlantic. This  
407 suggests that ENSO predictability decreases in the future in GFDL-ESM2M.

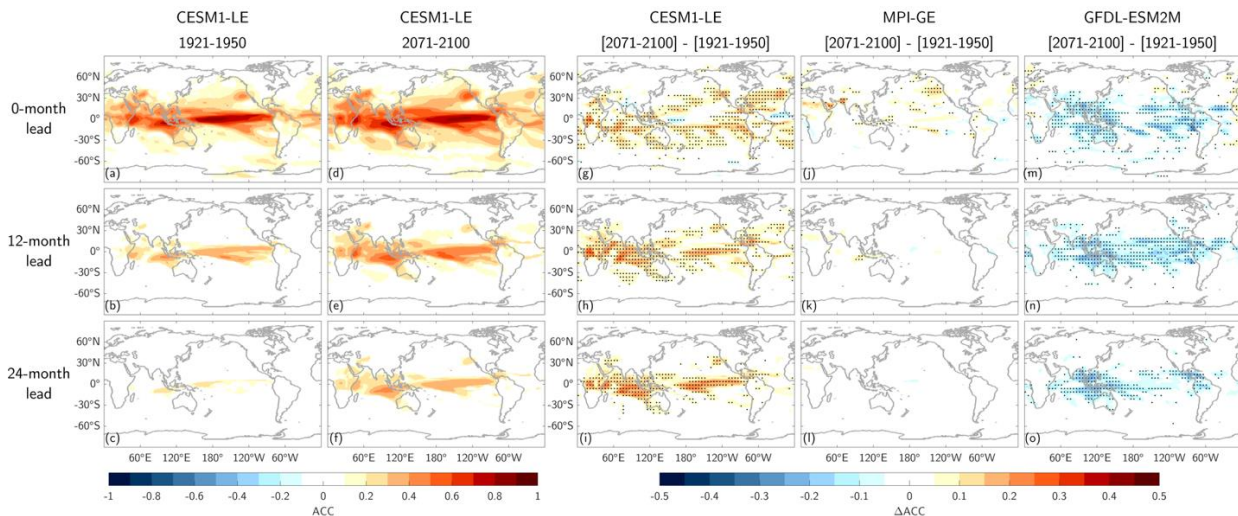
408

## 409 **2) Precipitation**

410 Forecasts of precipitation anomalies for 1921-1950 in CESM1-LE show peak skill over the  
411 tropical oceans (Figure 3a-c; see Figures S8-S12 for other models). For example, 0-month lead



412 precipitation skill is highest over the central equatorial Pacific, with ACCs exceeding 0.9. There  
 413 is also significant skill at 0-month lead over tropical land surfaces and in the mid-latitudes along  
 414 the U.S. west coast. Precipitation predictability similarly decreases with increasing lead, with only  
 415 the equatorial Pacific and Indian Oceans displaying any significant skill at 12-month lead. By 24-  
 416 month lead, precipitation predictability is generally insignificant, except for isolated regions in the  
 417 Indo-Pacific warm pool.  
 418



419  
 420 **Figure 3** As in Figure 2, but for precipitation predictability.  
 421

422 Similar to SSTA/SATA, there are robust increases in future precipitation predictability at  
 423 all leads in CESM1-LE (Figure 3d-i), with centers of action in the Indian Ocean, the equatorial  
 424 Pacific, the Caribbean, and the U.S. west coast. The North Atlantic also shows robust increases in  
 425 predictability at 0- and 12-month lead. The increase in predictability at 24-month lead is of particular  
 426 note given that there is virtually no significant skill in the past. In the future, however, there is  
 427 significant predictability over the equatorial Pacific and Indian Oceans. Additionally, the region  
 428 of highest skill along the equatorial Pacific shifts eastward from about the dateline in the period  
 429 1921-1950 to about 140°W in the period 2071-2100. This eastward shift may be related to CESM1-  
 430 LE simulated El Niño events shifting eastward in the future (O’Brien and Deser 2023; Williams  
 431 and Patricola 2018). The sign and relative magnitude of the skill changes in the other LEs are also  
 432 consistent with their respective SSTA/SATA predictability changes (Figure 3j-o). Specifically,  
 433 MPI-GE once again shows isolated regions of robust precipitation skill change at 0-month, but no

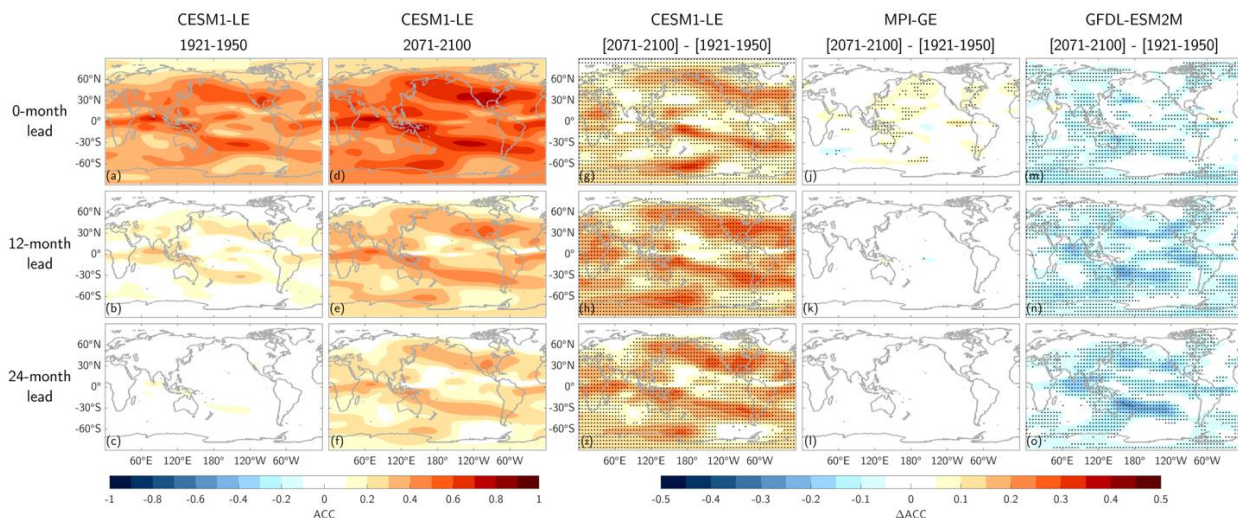


434 significant change at longer leads. Similarly, GFDL-ESM2M shows a robust decrease in  
 435 precipitation predictability at all leads throughout the tropics.

436

437 **3) Upper atmosphere circulation**

438 Forecasts of 500mb streamfunction anomalies ( $\psi_{500}$ ) during the period 1921-1950 in  
 439 CESM1-LE show significant skill at 0-month and 12-month leads (Figure 4a-c; see Figures S13-  
 440 S17 for other models). In particular, there are regions of high ACC in the subtropical and mid-  
 441 latitude North and South Pacific as well as over North America. These centers of action are  
 442 consistent with the locations of the PNA and Pacific-South American (PSA) patterns (Horel and  
 443 Wallace 1981; Mo and Ghil 1987). Combined, these two results suggest that the forecasts are  
 444 successfully capturing the upper atmospheric wave train response to tropical heating anomalies  
 445 associated with ENSO.



446

447 **Figure 4** As in Figure 2, but for 500mb streamfunction ( $\psi_{500}$ ) predictability.

448

449 In the future, there is a near-global increase in CESM1-LE  $\psi_{500}$  predictability at all leads  
 450 (Figure 4d-i). Of note are the increases in  $\psi_{500}$  ACC in the PNA and PSA regions, respectively,  
 451 which may be an indication of stronger ENSO teleconnections in CESM1-LE in the future  
 452 (O'Brien and Deser 2023). The robust predictability increases in the PNA region are also  
 453 consistent with the increases seen in both SSTA/SATA and precipitation predictability along the  
 454 U.S. west coast (see Figures 2g-i and 3g-i). Similar to precipitation forecasts, long-lead  $\psi_{500}$   
 455 predictability is especially impacted in CESM1-LE, with significant increases in predictability  
 456 nearly everywhere at 24-month lead. As with SSTA, SATA, and precipitation, the other LEs

457 disagree with CESM1-LE on the sign of future  $\psi_{500}$  predictability changes (Figure 4j-o). MPI-GE  
458 shows no regions of robust predictability changes beyond 0-month lead, and GFDL-ESM2M once  
459 again produces a decrease in  $\psi_{500}$  skill for most of the globe. In particular, GFDL-ESM2M shows  
460 a decrease in predictability in the PNA and PSA regions of the North and South Pacific, which  
461 may suggest that ENSO-related teleconnections in this model are weaker in the future.

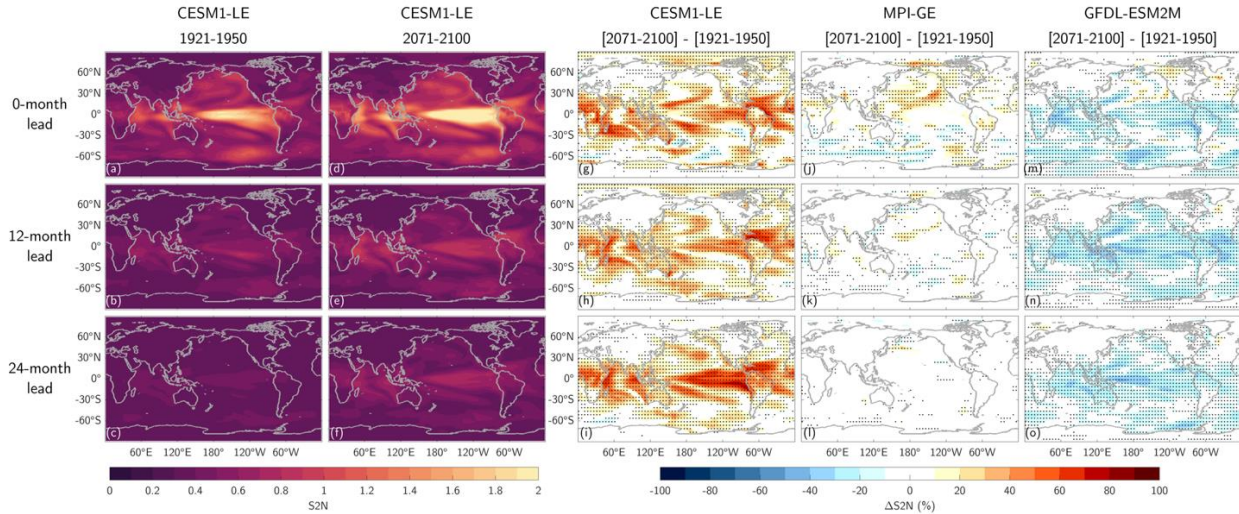
462

463 *(c) Linking future predictability changes and ENSO amplitude*

#### 464 **1) Signal-to-Noise**

465 To briefly summarize the above results, seasonal climate predictability in the future  
466 generally increases in CESM1-LE, does not change in MPI-GE, and decreases in GFDL-ESM2M,  
467 as measured by ACC across multiple variables (SSTA, SATA, precipitation, and  $\psi_{500}$ ). While the  
468 models disagree on the sign of future predictability changes, they are each self-consistent with  
469 their projected change in future ENSO amplitude (i.e., Figure 1). The link between future climate  
470 predictability and future ENSO amplitude may be related to ENSO's role as the dominant internal  
471 climate mode, allowing one to detect its influence across much of the globe despite the presence  
472 of other forms of variability (e.g., weather or other climate modes). For example, if ENSO  
473 amplitude increases in the future (e.g., as projected by CESM1-LE), then that may lead to an  
474 increase in the signal-to-noise (S2N) ratio of ENSO and its teleconnections, which would tend to  
475 contribute to an overall more deterministic climate system and more skillful forecasts (e.g.,  
476 Sardeshmukh et al., 2000). To test this hypothesis, we calculate changes in the S2N ratio (Eq. 1)  
477 for surface temperature as a function of lead time in each of the two time periods (Figure 5). During  
478 the period 1921-1950, the S2N ratios in CESM1-LE forecasts at 0-month lead follow an ENSO-  
479 like pattern, with the highest values in the equatorial Pacific (maximum value = 1.94). Weaker  
480 (but still elevated) values are seen in the Indian Ocean, the South Pacific, the Northeast Pacific  
481 along the U.S. west coast, the North Atlantic, and over the tropical African and South American  
482 land surfaces (Figure 5a). The S2N decreases with increasing lead time (Figure 5b-c); however,  
483 the ENSO-like pattern of elevated S2N persists at 12-month lead before mostly dissipating at 24-  
484 month lead.

485



486

487 **Figure 5** Signal-to-noise (S2N) ratios for surface temperature anomaly forecasts. (a)-(c) Ensemble mean S2N  
 488 of surface temperature forecasts in CESM1-LE calculated across all months in the period 1921-1950. (d)-(f) As  
 489 in (a)-(c), but for the period 2071-2100. (g)-(o) Percent change in S2N between past and future periods for (g)-  
 490 (i) CESM1-LE (j)-(l) MPI-GE (m)-(o) GFDL-ESM2M. Stipples in (g)-(o) indicate where 80% of a respective  
 491 model's ensemble agrees on the sign of the change.

492

493

494

495

496

497

498

499

500

501

502

503

504

505

506

507

508

509

510

The patterns of future S2N change in each of the LEs are remarkably similar to the surface temperature ACC changes seen in Figure 2 (Figure 5d-o), with pattern correlations between the ACC and S2N maps at 0-, 12-, and 24-month lead of 0.86, 0.97, and 0.98 for CESM1-LE, 0.76, 0.90, and 0.83 for MPI-GE, and 0.69, 0.95, and 0.95 for GFDL-ESM2M, respectively. Decomposing the S2N equation into a signal and noise component (i.e., the numerator and denominator of Eq. 1, respectively), we find that the changes in the signal are over five times larger than changes in the noise for much of the globe (Figures S18-S19). For example, the signal change averaged 60°S-60°N at 12-month lead in CESM1-LE is 27%, compared to just a 4.7% change in the noise. In the case of CESM1-LE, this indicates that the amplitude of a typical ensemble mean forecast anomaly is larger in the future without a substantial increase in the average forecast spread (i.e., the forecast uncertainty). These results are consistent with previous studies linking ENSO amplitude to S2N and/or climate predictability (Capotondi et al., 2015; Chen et al., 2004; Gu & Philander, 1997; Sardeshmukh et al., 2000; Suarez & Schopf, 1988; Weisheimer et al., 2022; Zhao et al., 2016).

507

## 508 2) Time-varying potential predictability changes, Nino3.4

509

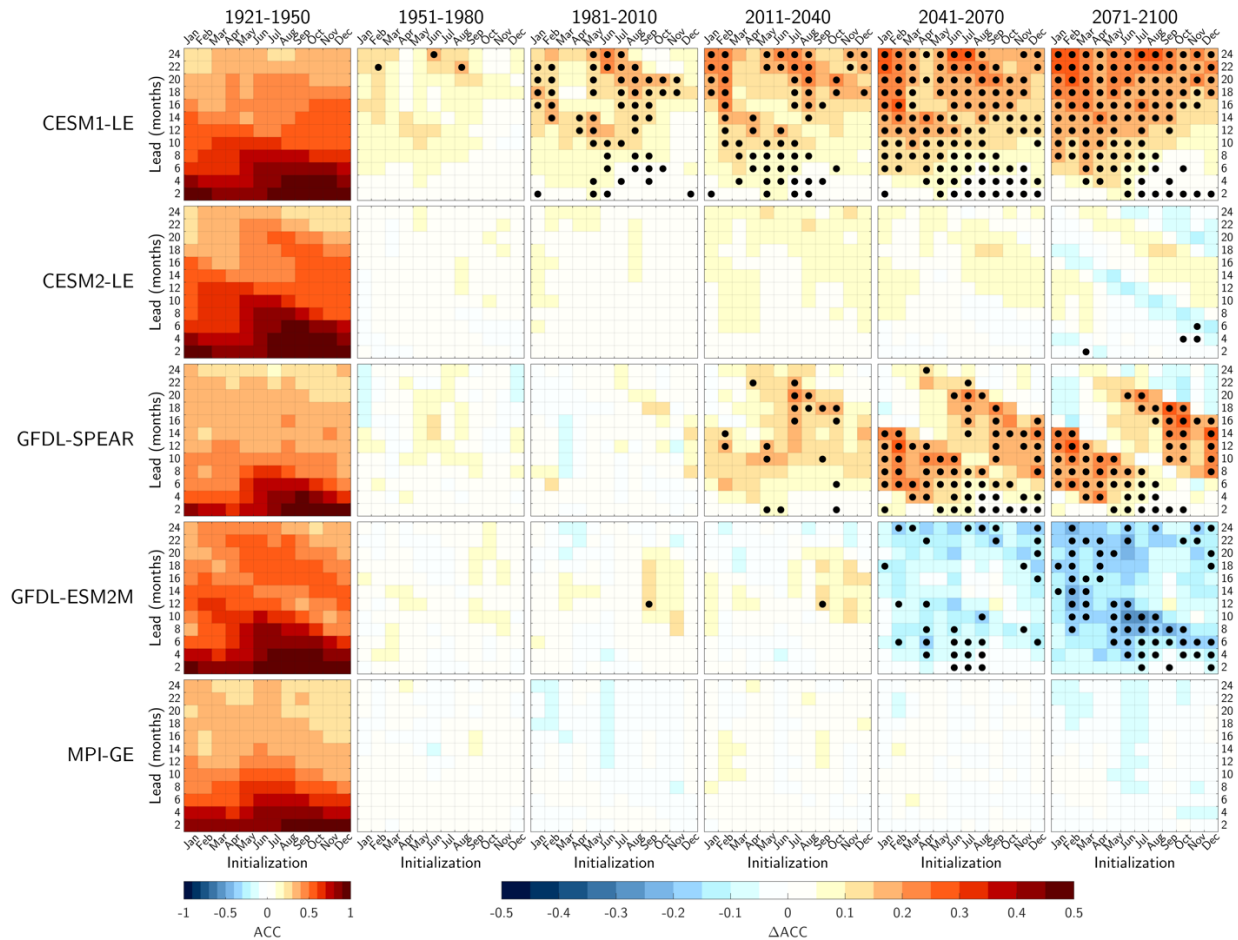
510

To further relate changes in ENSO amplitude to global predictability, we explore skill changes as a function of time. A time-varying perspective of predictability is important given the

511 non-monotonic changes in ENSO amplitude seen in most LEs (e.g., Figure 1). Such variability in  
512 each model’s forced ENSO response may give rise to periods of predictability that differ not only  
513 from the historical period, but also from the total changes seen at the end of the 21<sup>st</sup> century (i.e.,  
514 Figures 2-4). Further, by evaluating whether time-varying skill changes are robust across a given  
515 model’s ensemble, we can quantitatively estimate the “time of emergence” for forced changes in  
516 predictability within each model.

517 To illustrate, we show the forecast skill of SSTAs averaged in the Nino3.4 region for six  
518 different 30-year periods from 1921-2100 (Figure 6). In addition to CESM1-LE, MPI-GE, and  
519 GFDL-ESM2M, we also include CESM2-LE and GFDL-SPEAR in this analysis as ENSO  
520 amplitude changes in these models are particularly varied, with prolonged periods of increasing  
521 and decreasing variability. Treating 1921-1950 as the base period, Nino3.4 skill tends to be highest  
522 (exceeding 0.8) at leads of less than ~6 months and for forecasts initialized in boreal fall and winter  
523 (Figure 6; left column). For boreal spring and summer initializations, predictability tends to be  
524 similarly elevated at leads that encompass boreal winter in the forecast.

525



526

527 **Figure 6** First column: Ensemble mean Nino3.4 potential forecast skill (ACC) as a function of initialization  
 528 month (x-axis) and lead time (y-axis) for each model large ensemble. Second-fifth columns: Difference in  
 529 Nino3.4 skill between the base period 1921-1950 and different 30-year periods. For example, the second column  
 530 shows the difference in skill between the periods 1951-1980 and 1921-1950. Stipples indicate that 80% of the  
 531 respective model ensemble agrees on the sign of the change.

532

533

534

535

536

537

538

539

540

541

542

There is little change in Nino3.4 skill in any of the models for the adjacent 30-year period (1951-1980). However, by the period 1981-2010, CESM1-LE shows a robust increase in Nino3.4 predictability at short leads for May-September initializations and at longer leads for much of the year. This suggests that forced changes in CESM1-LE ENSO predictability begin to emerge above the internal noise inherent to each ensemble member during this period. In 2011-2040, CESM1-LE Nino3.4 skill continues to increase, while GFDL-SPEAR begins to show some robust increases in predictability. Forecast skill in CESM2 also increases slightly during this period, but there is not widespread agreement among its ensemble on the sign of this change. We see the largest period-to-period changes in Nino3.4 skill between 2011-2040 and 2041-2070 (Figure 6; fifth column). For example, forced changes to ENSO forecast skill in GFDL-SPEAR fully emerge



543 during this period, with diagonal bands of increased predictability associated with forecasts that  
544 verify in boreal summer to winter. In GFDL-ESM2M, robust decreases in predictability begin to  
545 emerge, but without a clear pattern. Finally, by the period 2071-2100, CESM1-LE and GFDL-  
546 SPEAR largely maintain the increases in ENSO predictability observed in the previous epoch,  
547 while forced decreases in Nino3.4 forecast skill are now fully evident in GFDL-ESM2M.

548

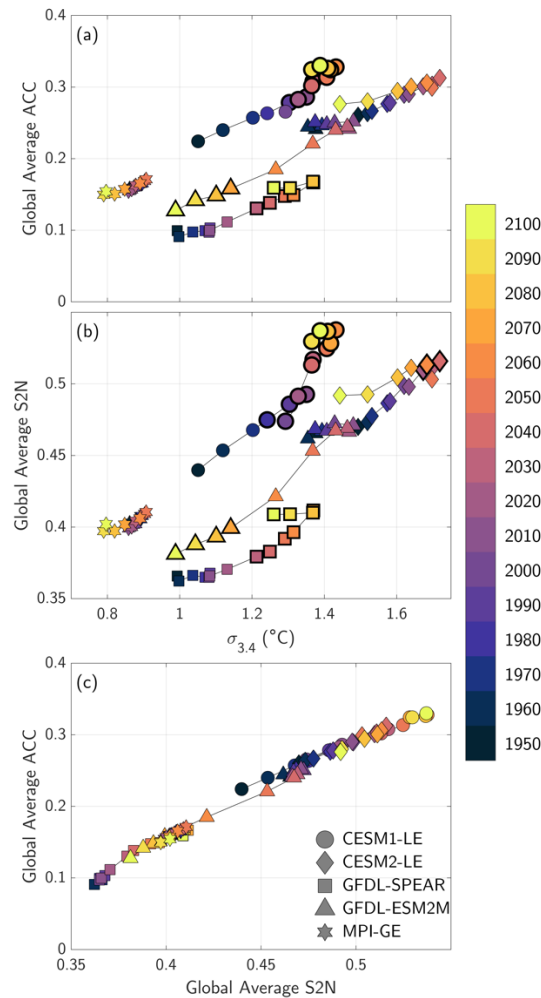
### 549 **3) Time-varying potential predictability changes, global**

550 There is clear model diversity in the simulated change of ENSO predictability, both in the  
551 sign and intensity of end-of-21<sup>st</sup> century changes and in the apparent time of emergence for each  
552 model's forced response (i.e., Figure 6 black dots). However, similar to our previous results (e.g.,  
553 Figures 2-4), the sign and timing of ENSO predictability changes in each of the LEs is consistent  
554 with their respective time-varying ENSO amplitudes (Figure 1). For example, there are no robust  
555 changes in Nino3.4 forecast skill in GFDL-SPEAR until the period 2011-2040, which closely  
556 corresponds to the timing of the strongest increasing trend in this model's ENSO amplitude  
557 (comparing third row of Figure 6 to orange line in Figure 1). Similarly, ENSO predictability in  
558 GFDL-ESM2M remains relatively stable until the period 2041-2070, at which point both the  
559 forecast skill and GFDL-ESM2M's ENSO amplitude start to sharply decrease (comparing fourth  
560 row of Figure 6 to purple line in Figure 1). The ensemble mean Nino3.4 skill in CESM2-LE also  
561 shows hints of a close link to its time-varying ENSO amplitude, with a slight increase in  
562 skill/amplitude through 2040 followed by a decrease through the end of the century, though these  
563 predictability changes are not robust across the CESM2 ensemble.

564 The relationship between time-varying ENSO amplitude and climate predictability extends  
565 beyond the Nino3.4 region, manifesting on global scales via ENSO-driven changes in the S2N  
566 ratio (as previously suggested in Figure 5). Indeed, we find a high correspondence in each LE  
567 between their respective time-evolving Nino3.4 amplitude, globally averaged ACC, and globally  
568 averaged S2N ratio (Figure 7). For example, at 12-month lead, the globally averaged SSTA skill  
569 in CESM1-LE increases roughly linearly over time with increasing ENSO amplitude (Figure 7a  
570 circles;  $R = 0.95$ ), with over 80% of the model ensemble agreeing on the sign of both the ENSO  
571 amplitude and global predictability changes beginning in the period 1961-1990 (i.e., circles with  
572 thick black outline). A similar linear relationship is seen in other LEs with different ENSO  
573 amplitude trends. For example, in GFDL-ESM2M, there is a decrease in skill over time that closely

574 corresponds to this model's decrease in ENSO amplitude (Figure 7a triangles;  $R = 0.97$ ), although  
 575 its forced changes in predictability are not apparent until the period 2031-2060.

576



577

578 **Figure 7** (a) Global average ensemble mean potential skill at 12-month lead (y-axis) versus December-February  
 579 averaged Nino3.4 standard deviation (x-axis) in different 30-year periods. (b) As in (a), but for global average  
 580 forecast S2N ratio versus Nino3.4 standard deviation. (c) As in (b), but for global average ACC versus global  
 581 average S2N ratio. All ACC and S2N values are based on ensemble mean SSTA forecasts from each model (i.e.,  
 582 different shapes). Shading of each shape indicates the 30-year window over which the forecast skill, S2N ratio  
 583 or Nino3.4 standard deviation are calculated, with the year indicating the end of the window. For example, the  
 584 shading for 1950 corresponds to 1921-1950. Markers with bold outlines in (a)-(b) indicate 30-year windows in  
 585 which 80% of a given model's ensemble agree on the sign of the change (relative to 1921-1950) for both the  
 586 ACC/S2N and Nino3.4 standard deviation.  
 587

588 Globally averaged S2N is also highly correlated in time with each model's projected ENSO  
 589 amplitude (Figure 7b), consistent with the S2N maps discussed earlier. There is also a near-perfect  
 590 linear relationship between globally averaged S2N and ACC (Figure 7c), consistent with previous  
 591 studies relating perfect model skill to S2N (Sardeshmukh et al. 2000). Finally, by calculating the

592 regression coefficient between globally averaged ACC/S2N and Nino3.4 amplitude (i.e., by fitting  
593 a line to each model's scatter in Figure 7a-b), we can estimate the skill/S2N changes for a given  
594 change in ENSO amplitude. Averaging the regression coefficients across models, we find that a  
595 10% increase in Nino3.4 amplitude is associated with a 14% and 7% increase in globally averaged  
596 forecast skill and S2N, respectively, at 12-month lead.

597 Combined, the results shown in Figure 7 further support our hypothesis that time-varying  
598 changes in predictability are driven by same-sign changes in global S2N ratios, which in turn are  
599 driven by each respective LE's projected change in ENSO amplitude. The close link between  
600 ENSO amplitude, S2N, and forecast skill is consistent across models (different marker types in  
601 Figure 7), lead times and variables (not shown).

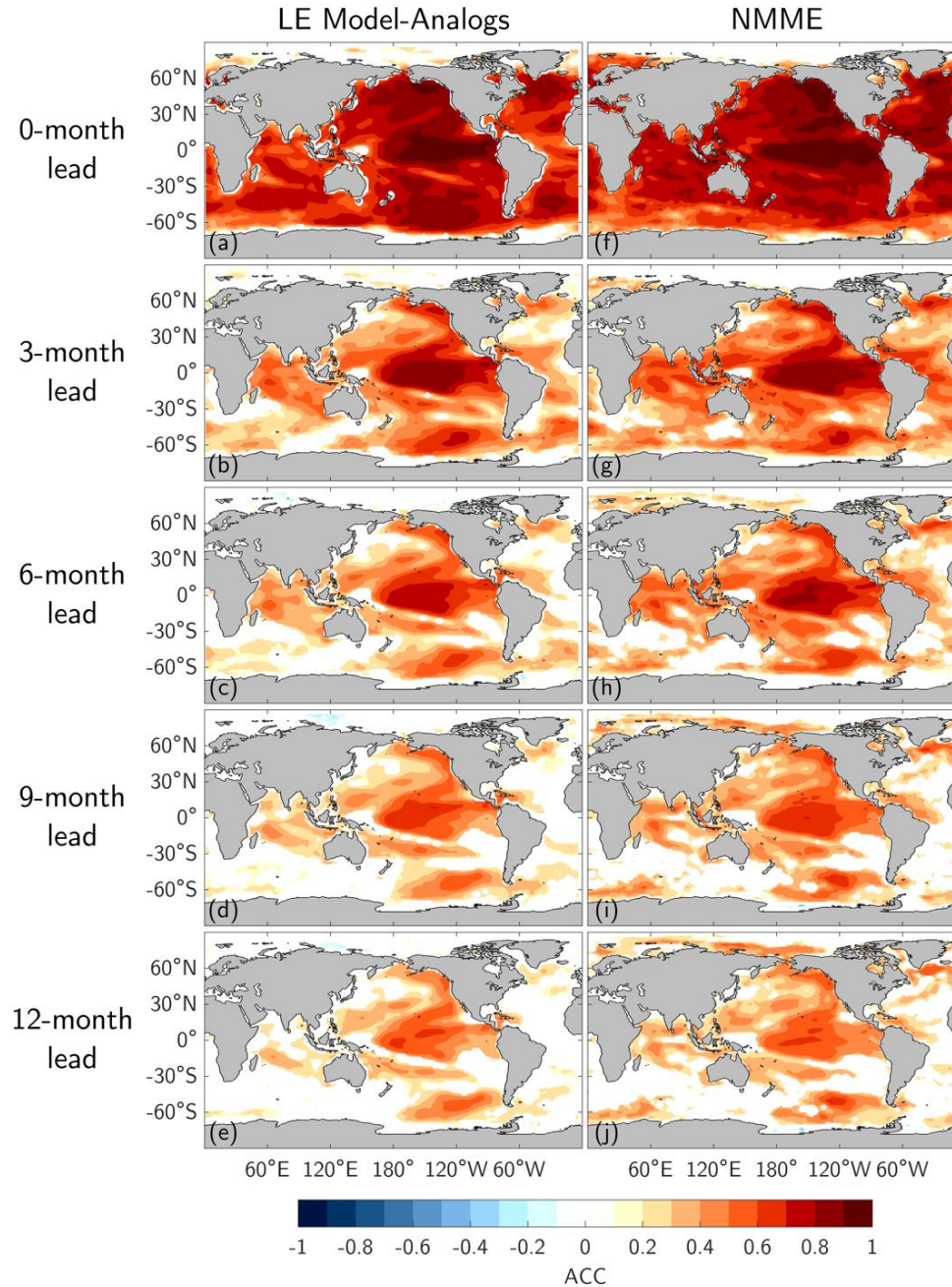
602

#### 603 *(d) Model-analog forecasts of the real world*

604 While our analysis to this point has focused on perfect model predictability in the past,  
605 present, and future, it is interesting to also consider whether model-analog forecasts drawn from  
606 LEs can skillfully predict the real world. Such an evaluation would provide an important  
607 assessment of whether these tools and techniques might be useful for real-world seasonal  
608 forecasting. For example, Ding and Alexander (2023) showed that, for much of the globe, model-  
609 analogs from CESM1-LE can predict observed SST variability in Years 2 and 3 at rates that match  
610 or even slightly exceed those from traditional initialized dynamical forecasts (see their Figure S2).  
611 However, to our knowledge, there are no studies that have quantified the hindcast skill of observed  
612 model-analogs drawn from a multi-model ensemble of LEs. Here, we present a preliminary  
613 verification of observed SSTA forecasts drawn from the five model LEs from 1991-2020.

614





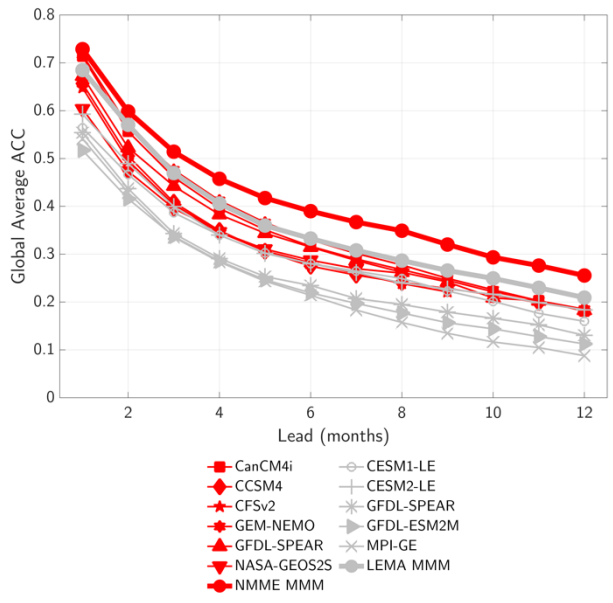
615  
616  
617  
618  
619  
620  
621

**Figure 8** Observed SSTA forecast skill from model-analogs and the NMME. (a)-(e) Seasonal skill of multi-model mean (MMM) model-analog forecasts drawn from each of the five model LEs. (f)-(j) As in (a)-(e), but the seasonal skill of MMM forecasts from the six NMME models. Skill is measured as ACC with observations from ERSSTv5 calculated across all months in the period 1991-2020. Skill values are only shown when 95% significant.

622 The multi-model mean (MMM) forecast from the five LEs shows significant skill at  
623 predicting real-world SSTAs at 0-month lead, indicating that the model-analog approach is  
624 accurately selecting climate states that are similar to the observations (Figure 8). As expected,

625 forecast skill of the observed model-analogs decreases everywhere with increasing lead time.  
 626 However, even at 12-months there is significant skill throughout the tropics, as well as in regions  
 627 well-known to be influenced by ENSO’s teleconnections (e.g., the Northeast Pacific). The LE  
 628 model-analog MMM skill compares favorably to MMM forecasts from traditional dynamical  
 629 forecasts contributing to the NMME, matching the NMME skill for much of the globe (Figure 8f-  
 630 j). While globally averaged model-analog skill from the individual LEs does tend to be lower than  
 631 globally averaged skill from individual NMME models (Figure 9), it is likely that the model-analog  
 632 skill could be further improved by optimizing the methods for selecting analogs. For example,  
 633 some studies have incorporated other variables (such as sea surface height) in addition to SST  
 634 when selecting analogs (Ding et al. 2018, 2019; Ding and Alexander 2023). Doing so may generate  
 635 analogs that more closely match the observed climate state over the length of the forecast, thereby  
 636 increasing skill. Similarly, other recent studies (Toride et al. in review; Rader & Barnes, 2023)  
 637 have used machine learning techniques to create spatial weights that are used to aid in analog  
 638 selection and are optimized to maximize forecast skill in a specific region (e.g., Nino3.4).  
 639 Regardless, the observed skill shown here further suggests that model-analog forecasts drawn from  
 640 free running climate simulations can provide reliable predictions comparable to state-of-the art  
 641 initialized forecasts, but at a fraction of the computational expense.

642



643 **Figure 9** Global average SSTA forecast skill for all months derived from dynamical forecasts from six NMME  
 644 models (red) and observed model-analog forecasts drawn from the five model LEs (gray). Skill is based on  
 645 comparisons to ERSSTv5 from 1991-2020. The MMM skill for NMME and the LE model-analogs (LEMA) are  
 646 shown in bold.  
 647

#### 648 **4. Summary and Discussion**

649 In this study, we investigated possible future changes in seasonal potential predictability  
650 across five coupled GCM LEs. Using a perfect model-analog technique, we generated hundreds  
651 of thousands of synthetic seasonal forecasts to estimate predictability changes from 1921-2100.  
652 CESM1-LE consistently showed a robust increase in predictability in the future, while  
653 predictability in GFDL-ESM2M consistently decreased (e.g., Figures 2-4). These predictability  
654 changes were largest at longer leads. In contrast, seasonal predictability in MPI-GE did not exhibit  
655 significant changes. This large inter-model uncertainty in the sign, magnitude, and timing of future  
656 climate predictability changes could be the result of any number of design choices unique to each  
657 modeling center, including different grid resolutions, parameterizations, physics packages, model  
658 components, or some combination thereof. Moreover, ENSO variance is a delicate balance  
659 between many competing processes, leading to uncertain forced changes in the near future (see  
660 Figure 1 of our study, as well as Maher et al., 2023; Cai et al., 2022; Yun et al., 2021; Fredriksen  
661 et al., 2020; Zheng et al., 2016; Stevenson, 2012; Collins et al., 2010; Latif & Keenlyside, 2009).  
662 However, this makes our central result even more striking—a common physical relationship  
663 among the models emerges that allows us to anticipate how real-world predictability might change  
664 in the coming decades. In particular, the predictability changes in each model were driven by a  
665 same-sign change in their respective ENSO amplitude. For example, forecasts from models with  
666 increasing ENSO amplitude trends (e.g., CESM1, GFDL-SPEAR, and CESM2 until ~2040) were  
667 associated with a higher S2N ratio in the future, which led to an overall more deterministic climate  
668 system and increased potential for significant forecast skill. The higher S2N ratio resulted from a  
669 larger ensemble mean forecast anomaly (i.e., signal), owing to ENSO’s role as a bigger “hammer”  
670 to the climate system. The opposite was true for models with decreasing ENSO trends (e.g., GFDL-  
671 ESM2M and CESM2 after ~2040). Overall, when averaged across models, a 10% increase in  
672 ENSO amplitude was associated with a 14% and 7% increase in globally averaged skill and S2N,  
673 respectively, at 12-month lead.

674 Of course, our study is based upon “perfect model” predictability analysis of imperfect  
675 climate models, with demonstrated mean and variability biases (e.g., Maher et al. 2023; Wills et  
676 al. 2022). While perfect model predictability is sometimes a reasonable proxy for “actual” skill  
677 (e.g., skill derived from a dynamical forecast system or traditional model-analog methods; Wheeler  
678 et al. 2017; Newman and Sardeshmukh 2017) this may not always be the case (e.g., Kumar et al.

679 2014; Weisheimer et al. 2022; Scaife and Smith 2018). As a result, we cannot necessarily expect  
680 that predictability changes in the remainder of this century will match future changes in the  
681 predictability of these models. Still, model-analog forecasts drawn from the LEs have comparable  
682 real-world SSTA skill (Figures 8-9) to that of operational seasonal forecast models (i.e., NMME),  
683 whose forecast errors are similar to climate model errors (e.g., Beverley et al. 2023). Therefore,  
684 our results are likely relevant to how prediction skill of current seasonal forecast systems might  
685 change in the future. For example, the observed trend in ENSO amplitude is positive since 1970  
686 (Figure 1). Should this trend persist into the future, we might also expect seasonal forecast skill to  
687 increase in regions strongly influenced by ENSO and its teleconnections as these portions of the  
688 climate system become more deterministic. However, if ENSO variability were to decrease in the  
689 future as suggested by several recent studies (Wengel et al. 2021; Callahan et al. 2021; Peng et al.  
690 in review), then historical forecast skill relationships that depend on ENSO and its teleconnections  
691 may become less reliable as the climate changes.

692 While our analysis takes an important first step towards understanding future climate  
693 predictability changes, there are a number of important questions that remain. First, is there a  
694 strong seasonality to future global predictability changes? Our study focused primarily on potential  
695 skill computed across all months; however, there were some seasonal differences in ENSO  
696 predictability changes (Figure 6). Additionally, Maher et al. (2023) showed that ENSO amplitude  
697 changes in the LEs analyzed here are stronger in some seasons (typically boreal winter) than others  
698 (see their Figure 4). Therefore, it is possible that ENSO's impact on future predictability may be  
699 seasonally dependent. Next, what other ENSO-related factors impact future climate predictability?  
700 Many studies have shown that ENSO frequency (e.g., Berner et al., 2020), flavor (i.e., central vs  
701 eastern Pacific; Capotondi et al., 2015), and asymmetry (i.e., the duration of El Niño versus La  
702 Niña events; Maher et al., 2023) may change in the future. Changes to these characteristics may  
703 alter ENSO's influence on the rest of the climate system and thereby climate predictability.  
704 Additionally, there may be changes in the background mean state (e.g., the strength of the east-  
705 west temperature gradient in the equatorial Pacific) that impact the overall climate response to  
706 ENSO (Cai et al. 2021). While we did not find a significant relationship between predictability in  
707 our forecasts and each LE's time-varying ENSO frequency or flavor preference (not shown), we  
708 encourage future studies to investigate these mechanisms in more detail.

709           Although ENSO is a dominant driver of seasonal forecast skill for much of the globe, there  
710 are likely other mechanisms that contribute to the predictability limits of different regions and  
711 variables. For example, Shi et al., (2022) showed that long-term shoaling of the mixed layer in the  
712 future may reduce the thermal inertia of the ocean, thereby decreasing ocean memory and year-to-  
713 year SST persistence, especially in the mid-latitudes. Similarly, Kumar et al., (2023) found that  
714 global warming decreases soil moisture memory over North America due to an increase in  
715 potential evapotranspiration. In both cases, the reduction in climate memory increases variability  
716 at less predictable high frequencies (e.g., weather timescales) while decreasing variability at lower  
717 frequencies (e.g., seasonal and longer), thus “whitening” the power spectrum and contributing to  
718 a decrease in persistence-related predictability. However, it is still unclear to what extent these  
719 changes may be offset by dynamical drivers of predictability change related to ENSO. More  
720 research is needed to unpack the dynamic versus thermodynamic contributions to future climate  
721 predictability change.

722

## 723 **Acknowledgements**

724 We thank Friedrich Burger and Thomas Frölicher for providing us with the GFDL-ESM2M data  
725 used in this study. We also thank two anonymous reviewers for their insightful comments and  
726 suggestions that improved the quality of this work. This research was supported in part by the  
727 Australian Research Council Discovery Early Career Researcher Award DE230100315 and  
728 the NOAA cooperative agreement NA22OAR4320151.

729

## 730 **Data Availability Statement**

731 Large ensemble datasets are available as follows:

732 CESM1-LE: <https://www.cesm.ucar.edu/projects/community-projects/MMLEA/>

733 CESM2-LE: <https://www.cesm.ucar.edu/projects/community-projects/LENS2/>

734 GFDL-SPEAR: [https://www.gfdl.noaa.gov/spear\\_large\\_ensembles/](https://www.gfdl.noaa.gov/spear_large_ensembles/)

735 GFDL-ESM2M: Provided by Friedrich Burger and Thomas Frölicher at the University of Bern.

736 MPI-GE: <https://esgf-data.dkrz.de/projects/mpi-ge/>

737 ERSSTv5, COBE, and COBE2 are available at <https://psl.noaa.gov/data/gridded/tables/sst.html>

738 HadISST data are available at <https://www.metoffice.gov.uk/hadobs/hadisst/data/download.html>

739 **References**

- 740 Barnett, T. P., and R. Preisendorfer, 1987: Origins and Levels of Monthly and Seasonal Forecast  
741 Skill for United States Surface Air Temperatures Determined by Canonical Correlation  
742 Analysis. *Monthly Weather Review*, **115**, 1825–1850, [https://doi.org/10.1175/1520-0493\(1987\)115<1825:OALOMA>2.0.CO;2](https://doi.org/10.1175/1520-0493(1987)115<1825:OALOMA>2.0.CO;2).  
743
- 744 Barnston, A. G., and M. K. Tippett, 2017: Do Statistical Pattern Corrections Improve Seasonal  
745 Climate Predictions in the North American Multimodel Ensemble Models? *Journal of*  
746 *Climate*, **30**, 8335–8355, <https://doi.org/10.1175/JCLI-D-17-0054.1>.
- 747 ———, ———, M. L. L’Heureux, S. Li, and D. G. DeWitt, 2012: Skill of Real-Time Seasonal  
748 ENSO Model Predictions during 2002–11: Is Our Capability Increasing? *Bulletin of the*  
749 *American Meteorological Society*, **93**, 631–651, <https://doi.org/10.1175/BAMS-D-11-00111.1>.  
750
- 751 Becker, E., H. van den Dool, and Q. Zhang, 2014: Predictability and Forecast Skill in NMME.  
752 *Journal of Climate*, **27**, 5891–5906, <https://doi.org/10.1175/JCLI-D-13-00597.1>.
- 753 Becker, E. J., B. P. Kirtman, M. L’Heureux, Á. G. Muñoz, and K. Pegion, 2022: A Decade of the  
754 North American Multimodel Ensemble (NMME): Research, Application, and Future  
755 Directions. *Bulletin of the American Meteorological Society*, **103**, E973–E995,  
756 <https://doi.org/10.1175/BAMS-D-20-0327.1>.
- 757 Berner, J., H. M. Christensen, and P. D. Sardeshmukh, 2020: Does ENSO Regularity Increase in  
758 a Warming Climate? *Journal of Climate*, **33**, 1247–1259, <https://doi.org/10.1175/JCLI-D-19-0545.1>.  
759
- 760 Beverley, J. D., M. Newman, and A. Hoell, 2023: Rapid Development of Systematic ENSO-  
761 Related Seasonal Forecast Errors. *Geophysical Research Letters*, **50**, e2022GL102249,  
762 <https://doi.org/10.1029/2022GL102249>.
- 763 Burger, F. A., J. G. John, and T. L. Frölicher, 2020: Increase in ocean acidity variability and  
764 extremes under increasing atmospheric CO<sub>2</sub>. *Biogeosciences*, **17**, 4633–4662,  
765 <https://doi.org/10.5194/bg-17-4633-2020>.
- 766 ———, J. Terhaar, and T. L. Frölicher, 2022: Compound marine heatwaves and ocean acidity  
767 extremes. *Nat Commun*, **13**, 4722, <https://doi.org/10.1038/s41467-022-32120-7>.
- 768 Cai, W., and Coauthors, 2021: Changing El Niño–Southern Oscillation in a warming climate.  
769 *Nat Rev Earth Environ*, **2**, 628–644, <https://doi.org/10.1038/s43017-021-00199-z>.
- 770 ———, B. Ng, G. Wang, A. Santoso, L. Wu, and K. Yang, 2022: Increased ENSO sea surface  
771 temperature variability under four IPCC emission scenarios. *Nat. Clim. Chang.*, **12**, 228–  
772 231, <https://doi.org/10.1038/s41558-022-01282-z>.

- 773 Callahan, C. W., C. Chen, M. Rugenstein, J. Bloch-Johnson, S. Yang, and E. J. Moyer, 2021:  
774 Robust decrease in El Niño/Southern Oscillation amplitude under long-term warming.  
775 *Nat. Clim. Chang.*, **11**, 752–757, <https://doi.org/10.1038/s41558-021-01099-2>.
- 776 Capotondi, A., and Coauthors, 2015: Understanding ENSO diversity. *Bulletin of the American  
777 Meteorological Society*, **96**, 921–938, <https://doi.org/10.1175/BAMS-D-13-00117.1>.
- 778 Chen, D., M. A. Cane, A. Kaplan, S. E. Zebiak, and D. Huang, 2004: Predictability of El Niño  
779 over the past 148 years. *Nature*, **428**, 733–736, <https://doi.org/10.1038/nature02439>.
- 780 Collins, M., and Coauthors, 2010: The impact of global warming on the tropical Pacific Ocean  
781 and El Niño. *Nature Geosci*, **3**, 391–397, <https://doi.org/10.1038/ngeo868>.
- 782 Delworth, T. L., and Coauthors, 2020: SPEAR: The Next Generation GFDL Modeling System  
783 for Seasonal to Multidecadal Prediction and Projection. *Journal of Advances in Modeling  
784 Earth Systems*, **12**, e2019MS001895, <https://doi.org/10.1029/2019MS001895>.
- 785 Derome, J., H. Lin, and G. Brunet, 2005: Seasonal Forecasting with a Simple General  
786 Circulation Model: Predictive Skill in the AO and PNA. *Journal of Climate*, **18**, 597–  
787 609, <https://doi.org/10.1175/JCLI-3289.1>.
- 788 Ding, H., and M. A. Alexander, 2023: Multi-Year Predictability of Global Sea Surface  
789 Temperature Using Model-Analogs. *Geophysical Research Letters*, **50**, e2023GL104097,  
790 <https://doi.org/10.1029/2023GL104097>.
- 791 ———, M. Newman, M. A. Alexander, and A. T. Wittenberg, 2018: Skillful Climate Forecasts of  
792 the Tropical Indo-Pacific Ocean Using Model-Analogs. *Journal of Climate*, **31**, 5437–  
793 5459, <https://doi.org/10.1175/JCLI-D-17-0661.1>.
- 794 ———, ———, ———, and ———, 2019: Diagnosing Secular Variations in Retrospective ENSO  
795 Seasonal Forecast Skill Using CMIP5 Model-Analogs. *Geophysical Research Letters*, **46**,  
796 1721–1730, <https://doi.org/10.1029/2018GL080598>.
- 797 Fredriksen, H.-B., J. Berner, A. C. Subramanian, and A. Capotondi, 2020: How Does El Niño–  
798 Southern Oscillation Change Under Global Warming—A First Look at CMIP6.  
799 *Geophysical Research Letters*, **47**, e2020GL090640,  
800 <https://doi.org/10.1029/2020GL090640>.
- 801 Gan, B., L. Wu, F. Jia, S. Li, W. Cai, H. Nakamura, M. A. Alexander, and A. J. Miller, 2017: On  
802 the Response of the Aleutian Low to Greenhouse Warming. *Journal of Climate*, **30**,  
803 3907–3925, <https://doi.org/10.1175/JCLI-D-15-0789.1>.
- 804 Gu, D., and S. G. H. Philander, 1997: Interdecadal climate fluctuations that depend on exchanges  
805 between the tropics and extratropics. *Science*, **275**, 805–807,  
806 <https://doi.org/10.1126/science.275.5301.805>.

- 807 He, S., J.-Y. Yu, S. Yang, and S.-W. Fang, 2020: ENSO's impacts on the tropical Indian and  
808 Atlantic Oceans via tropical atmospheric processes: observations versus CMIP5  
809 simulations. *Clim Dyn*, **54**, 4627–4640, <https://doi.org/10.1007/s00382-020-05247-w>.
- 810 Heede, U. K., and A. V. Fedorov, 2023: Towards understanding the robust strengthening of  
811 ENSO and more frequent extreme El Niño events in CMIP6 global warming simulations.  
812 *Clim Dyn*, **61**, 3047–3060, <https://doi.org/10.1007/s00382-023-06856-x>.
- 813 Hirahara, S., M. Ishii, and Y. Fukuda, 2014: Centennial-Scale Sea Surface Temperature Analysis  
814 and Its Uncertainty. *Journal of Climate*, **27**, 57–75, <https://doi.org/10.1175/JCLI-D-12-00837.1>.
- 816 Horel, J. D., and J. M. Wallace, 1981: Planetary-scale phenomena associated with the Southern  
817 Oscillation. *Mon. Wea. Rev.*, **109**, 813–829, [https://doi.org/10.1175/1520-0493\(1981\)109<0813:PSAPAW>2.0.CO;2](https://doi.org/10.1175/1520-0493(1981)109<0813:PSAPAW>2.0.CO;2).
- 819 Huang, B., and Coauthors, 2017: Extended reconstructed Sea surface temperature, Version 5  
820 (ERSSTv5): Upgrades, validations, and intercomparisons. *Journal of Climate*, **30**, 8179–  
821 8205, <https://doi.org/10.1175/JCLI-D-16-0836.1>.
- 822 Ishii, M., A. Shouji, S. Sugimoto, and T. Matsumoto, 2005: Objective analyses of sea-surface  
823 temperature and marine meteorological variables for the 20th century using ICOADS and  
824 the Kobe Collection. *International Journal of Climatology*, **25**, 865–879,  
825 <https://doi.org/10.1002/joc.1169>.
- 826 Jacox, M. G., M. A. Alexander, C. A. Stock, and G. Hervieux, 2019: On the skill of seasonal sea  
827 surface temperature forecasts in the California Current System and its connection to  
828 ENSO variability. *Climate Dynamics*, **53**, 7519–7533, <https://doi.org/10.1007/s00382-017-3608-y>.
- 830 Kay, J. E., and Coauthors, 2015: The community earth system model (CESM) large ensemble  
831 project : A community resource for studying climate change in the presence of internal  
832 climate variability. *Bulletin of the American Meteorological Society*, **96**, 1333–1349,  
833 <https://doi.org/10.1175/BAMS-D-13-00255.1>.
- 834 Kirtman, B. P., and P. S. Schopf, 1998: Decadal Variability in ENSO Predictability and  
835 Prediction. *Journal of Climate*, **11**, 2804–2822, [https://doi.org/10.1175/1520-0442\(1998\)011<2804:DVIEPA>2.0.CO;2](https://doi.org/10.1175/1520-0442(1998)011<2804:DVIEPA>2.0.CO;2).
- 837 ———, and Coauthors, 2014: The North American multimodel ensemble: Phase-1 seasonal-to-  
838 interannual prediction; phase-2 toward developing intraseasonal prediction. *Bulletin of  
839 the American Meteorological Society*, **95**, 585–601, <https://doi.org/10.1175/BAMS-D-12-00050.1>.
- 841 Kumar, A., 2009: Finite Samples and Uncertainty Estimates for Skill Measures for Seasonal  
842 Prediction. *Monthly Weather Review*, **137**, 2622–2631,  
843 <https://doi.org/10.1175/2009MWR2814.1>.



- 844 ———, P. Peng, and M. Chen, 2014: Is There a Relationship between Potential and Actual Skill?  
845 *Monthly Weather Review*, **142**, 2220–2227, <https://doi.org/10.1175/MWR-D-13-00287.1>.
- 846 Kumar, S., C. F. Dewes, M. Newman, and Y. Duan, 2023: Robust Changes in North America’s  
847 Hydroclimate Variability and Predictability. *Earth’s Future*, **11**, e2022EF003239,  
848 <https://doi.org/10.1029/2022EF003239>.
- 849 Kushnir, Y., W. A. Robinson, P. Chang, and A. W. Robertson, 2006: The Physical Basis for  
850 Predicting Atlantic Sector Seasonal-to-Interannual Climate Variability. *Journal of*  
851 *Climate*, **19**, 5949–5970, <https://doi.org/10.1175/JCLI3943.1>.
- 852 Latif, M., and N. S. Keenlyside, 2009: El Niño/Southern Oscillation response to global warming.  
853 *Proceedings of the National Academy of Sciences*, **106**, 20578–20583,  
854 <https://doi.org/10.1073/pnas.0710860105>.
- 855 Lorenz, E. N., 1969: Atmospheric Predictability as Revealed by Naturally Occurring Analogues.  
856 *Journal of the Atmospheric Sciences*, **26**, 636–646, [https://doi.org/10.1175/1520-0469\(1969\)26<636:APARBN>2.0.CO;2](https://doi.org/10.1175/1520-0469(1969)26<636:APARBN>2.0.CO;2).
- 858 Lou, J., M. Newman, and A. Hoell, 2023: Multi-decadal variation of ENSO forecast skill since  
859 the late 1800s. *npj Clim Atmos Sci*, **6**, 1–14, <https://doi.org/10.1038/s41612-023-00417-z>.
- 860 MacLeod, D., C. O’Reilly, T. Palmer, and A. Weisheimer, 2018: Flow dependent ensemble  
861 spread in seasonal forecasts of the boreal winter extratropics. *Atmospheric Science*  
862 *Letters*, **19**, e815, <https://doi.org/10.1002/asl.815>.
- 863 Maher, N., and Coauthors, 2019: The Max Planck Institute Grand Ensemble - Enabling the  
864 Exploration of Climate System Variability. *Journal of Advances in Modeling Earth*  
865 *Systems*, 2019MS001639, <https://doi.org/10.1029/2019MS001639>.
- 866 ———, S. Milinski, and R. Ludwig, 2021: Large ensemble climate model simulations:  
867 introduction, overview, and future prospects for utilising multiple types of large  
868 ensemble. *Earth System Dynamics*, **12**, 401–418, [https://doi.org/10.5194/esd-12-401-](https://doi.org/10.5194/esd-12-401-2021)  
869 2021.
- 870 ———, and Coauthors, 2023: The future of the El Niño–Southern Oscillation: using large  
871 ensembles to illuminate time-varying responses and inter-model differences. *Earth*  
872 *System Dynamics*, **14**, 413–431, <https://doi.org/10.5194/esd-14-413-2023>.
- 873 McGregor, S., C. Cassou, Y. Kosaka, and A. S. Phillips, 2022: Projected ENSO Teleconnection  
874 Changes in CMIP6. *Geophysical Research Letters*, **49**, e2021GL097511,  
875 <https://doi.org/10.1029/2021GL097511>.
- 876 Mo, K. C., and M. Ghil, 1987: Statistics and Dynamics of Persistent Anomalies. *Journal of the*  
877 *Atmospheric Sciences*, **44**, 877–902, [https://doi.org/10.1175/1520-0469\(1987\)044<0877:SADOPA>2.0.CO;2](https://doi.org/10.1175/1520-0469(1987)044<0877:SADOPA>2.0.CO;2).

- 879 Newman, M., and P. D. Sardeshmukh, 2017: Are we near the predictability limit of tropical  
880 Indo-Pacific sea surface temperatures? *Geophysical Research Letters*, **44**, 8520–8529,  
881 <https://doi.org/10.1002/2017GL074088>.
- 882 O’Brien, J. P., and C. Deser, 2023: Quantifying and Understanding Forced Changes to Unforced  
883 Modes of Atmospheric Circulation Variability over the North Pacific in a Coupled Model  
884 Large Ensemble. *Journal of Climate*, **36**, 19–37, <https://doi.org/10.1175/JCLI-D-22-0101.1>.
- 886 O’Reilly, C. H., J. Heatley, D. MacLeod, A. Weisheimer, T. N. Palmer, N. Schaller, and T.  
887 Woollings, 2017: Variability in seasonal forecast skill of Northern Hemisphere winters  
888 over the twentieth century. *Geophysical Research Letters*, **44**, 5729–5738,  
889 <https://doi.org/10.1002/2017GL073736>.
- 890 ———, T. Woollings, L. Zanna, and A. Weisheimer, 2019: An Interdecadal Shift of the  
891 Extratropical Teleconnection From the Tropical Pacific During Boreal Summer.  
892 *Geophysical Research Letters*, **46**, 13379–13388,  
893 <https://doi.org/10.1029/2019GL084079>.
- 894 Peng, Q., S.-P. Xie, and C. Deser. Collapsed upwelling weakens ENSO under sustained warming  
895 beyond the 21<sup>st</sup> century. *In review*.
- 896  
897 Power, S., and Coauthors, 2021: Decadal climate variability in the tropical Pacific:  
898 Characteristics, causes, predictability, and prospects. *Science*, **374**, eaay9165,  
899 <https://doi.org/10.1126/science.aay9165>.
- 900 Quan, X., M. Hoerling, J. Whitaker, G. Bates, and T. Xu, 2006: Diagnosing Sources of U.S.  
901 Seasonal Forecast Skill. *Journal of Climate*, **19**, 3279–3293,  
902 <https://doi.org/10.1175/JCLI3789.1>.
- 903 Rader, J. K., and E. A. Barnes, 2023: Optimizing Seasonal-To-Decadal Analog Forecasts With a  
904 Learned Spatially-Weighted Mask. *Geophysical Research Letters*, **50**, e2023GL104983,  
905 <https://doi.org/10.1029/2023GL104983>.
- 906 Rayner, N. A., D. E. Parker, E. B. Horton, C. K. Folland, L. V. Alexander, D. P. Rowell, E. C.  
907 Kent, and A. Kaplan, 2003: Global analyses of sea surface temperature, sea ice, and night  
908 marine air temperature since the late nineteenth century. *J. Geophys. Res.*, **108**,  
909 2002JD002670, <https://doi.org/10.1029/2002JD002670>.
- 910 Rodgers, K. B., and Coauthors, 2021: Ubiquity of human-induced changes in climate variability.  
911 *Earth System Dynamics*, **12**, 1393–1411, <https://doi.org/10.5194/esd-12-1393-2021>.
- 912 Sardeshmukh, P. D., G. P. Compo, and C. Penland, 2000: Changes of Probability Associated  
913 with El Niño. *Journal of Climate*, **13**, 4268–4286, [https://doi.org/10.1175/1520-0442\(2000\)013<4268:COPAWE>2.0.CO;2](https://doi.org/10.1175/1520-0442(2000)013<4268:COPAWE>2.0.CO;2).
- 914  
915 Scaife, A. A., and D. Smith, 2018: A signal-to-noise paradox in climate science. *npj Clim Atmos*  
916 *Sci*, **1**, 1–8, <https://doi.org/10.1038/s41612-018-0038-4>.

- 917 Shi, H., and Coauthors, 2022: Global decline in ocean memory over the 21st century. *Science*  
918 *Advances*, **8**, eabm3468, <https://doi.org/10.1126/sciadv.abm3468>.
- 919 Shi, W., N. Schaller, D. MacLeod, T. N. Palmer, and A. Weisheimer, 2015: Impact of hindcast  
920 length on estimates of seasonal climate predictability. *Geophysical Research Letters*, **42**,  
921 1554–1559, <https://doi.org/10.1002/2014GL062829>.
- 922 Stevenson, S. L., 2012: Significant changes to ENSO strength and impacts in the twenty-first  
923 century: Results from CMIP5. *Geophysical Research Letters*, **39**,  
924 <https://doi.org/10.1029/2012GL052759>.
- 925 Storch, H. von, and F. W. Zwiers, 1999: *Statistical Analysis in Climate Research*. Cambridge  
926 University Press,.
- 927 Suarez, M. J., and P. S. Schopf, 1988: A Delayed Action Oscillator for ENSO. *Journal of the*  
928 *Atmospheric Sciences*, **45**, 3283–3287, [https://doi.org/10.1175/1520-  
929 0469\(1988\)045<3283:ADAOFE>2.0.CO;2](https://doi.org/10.1175/1520-0469(1988)045<3283:ADAOFE>2.0.CO;2).
- 930 Toride, K., M. Newman, A. Capotondi, J. Schlör, D. J. Amaya, and A. Hoell. Interpretable ENSO  
931 forecasting using a hybrid deep learning analog approach. *In review*.  
932
- 933 Weisheimer, A., N. Schaller, C. O'Reilly, D. A. MacLeod, and T. Palmer, 2017: Atmospheric  
934 seasonal forecasts of the twentieth century: multi-decadal variability in predictive skill of  
935 the winter North Atlantic Oscillation (NAO) and their potential value for extreme event  
936 attribution. *Quarterly Journal of the Royal Meteorological Society*, **143**, 917–926,  
937 <https://doi.org/10.1002/qj.2976>.
- 938 ———, D. Decremmer, D. MacLeod, C. O'Reilly, T. N. Stockdale, S. Johnson, and T. N. Palmer,  
939 2019: How confident are predictability estimates of the winter North Atlantic  
940 Oscillation? *Quarterly Journal of the Royal Meteorological Society*, **145**, 140–159,  
941 <https://doi.org/10.1002/qj.3446>.
- 942 ———, D. J. Belfort, D. MacLeod, T. Palmer, C. O'Reilly, and K. Strømmen, 2020: Seasonal  
943 Forecasts of the Twentieth Century. *Bulletin of the American Meteorological Society*,  
944 **101**, E1413–E1426, <https://doi.org/10.1175/BAMS-D-19-0019.1>.
- 945 ———, M. A. Balmaseda, T. N. Stockdale, M. Mayer, S. Sharmila, H. Hendon, and O. Alves,  
946 2022: Variability of ENSO Forecast Skill in 2-Year Global Reforecasts Over the 20th  
947 Century. *Geophysical Research Letters*, **49**, e2022GL097885,  
948 <https://doi.org/10.1029/2022GL097885>.
- 949 ———, and Coauthors, 2024: The Signal-to-Noise Paradox in Climate Forecasts: Revisiting our  
950 Understanding and Identifying Future Priorities. *Bulletin of the American Meteorological*  
951 *Society*, **1**, <https://doi.org/10.1175/BAMS-D-24-0019.1>.
- 952 Wengel, C., S.-S. Lee, M. F. Stuecker, A. Timmermann, J.-E. Chu, and F. Schloesser, 2021:  
953 Future high-resolution El Niño/Southern Oscillation dynamics. *Nat. Clim. Chang.*, **11**,  
954 758–765, <https://doi.org/10.1038/s41558-021-01132-4>.

- 955 Wheeler, M. C., H. Zhu, A. H. Sobel, D. Hudson, and F. Vitart, 2017: Seamless precipitation  
956 prediction skill comparison between two global models. *Quarterly Journal of the Royal*  
957 *Meteorological Society*, **143**, 374–383, <https://doi.org/10.1002/qj.2928>.
- 958 Williams, I. N., and C. M. Patricola, 2018: Diversity of ENSO Events Unified by Convective  
959 Threshold Sea Surface Temperature: A Nonlinear ENSO Index. *Geophysical Research*  
960 *Letters*, **45**, 9236–9244, <https://doi.org/10.1029/2018GL079203>.
- 961 Wills, R. C. J., Y. Dong, C. Proistosescu, K. C. Armour, and D. S. Battisti, 2022: Systematic  
962 Climate Model Biases in the Large-Scale Patterns of Recent Sea-Surface Temperature  
963 and Sea-Level Pressure Change. *Geophysical Research Letters*, **49**, e2022GL100011,  
964 <https://doi.org/10.1029/2022GL100011>.
- 965 Wittenberg, A. T., A. Rosati, T. L. Delworth, G. A. Vecchi, and F. Zeng, 2014: ENSO  
966 Modulation: Is It Decadally Predictable? *Journal of Climate*, **27**, 2667–2681,  
967 <https://doi.org/10.1175/JCLI-D-13-00577.1>.
- 968 Yun, K.-S., J.-Y. Lee, A. Timmermann, K. Stein, M. F. Stuecker, J. C. Fyfe, and E.-S. Chung,  
969 2021: Increasing ENSO–rainfall variability due to changes in future tropical temperature–  
970 rainfall relationship. *Commun Earth Environ*, **2**, 1–7, [https://doi.org/10.1038/s43247-021-](https://doi.org/10.1038/s43247-021-00108-8)  
971 [00108-8](https://doi.org/10.1038/s43247-021-00108-8).
- 972 Zhao, M., H. H. Hendon, O. Alves, G. Liu, and G. Wang, 2016: Weakened Eastern Pacific El  
973 Niño Predictability in the Early Twenty-First Century. *Journal of Climate*, **29**, 6805–  
974 6822, <https://doi.org/10.1175/JCLI-D-15-0876.1>.
- 975 Zheng, X.-T., S.-P. Xie, L.-H. Lv, and Z.-Q. Zhou, 2016: Intermodel Uncertainty in ENSO  
976 Amplitude Change Tied to Pacific Ocean Warming Pattern. *Journal of Climate*, **29**,  
977 7265–7279, <https://doi.org/10.1175/JCLI-D-16-0039.1>.
- 978 Zheng, Y., M. Rugenstein, P. Pieper, G. Beobide-Arsuaga, and J. Baehr, 2022: El Niño–Southern  
979 Oscillation (ENSO) predictability in equilibrated warmer climates. *Earth System*  
980 *Dynamics*, **13**, 1611–1623, <https://doi.org/10.5194/esd-13-1611-2022>.
- 981 Zhou, Z.-Q., S.-P. Xie, X.-T. Zheng, Q. Liu, and H. Wang, 2014: Global Warming–Induced  
982 Changes in El Niño Teleconnections over the North Pacific and North America. *Journal*  
983 *of Climate*, **27**, 9050–9064, <https://doi.org/10.1175/JCLI-D-14-00254.1>.
- 984



Click here to access/download

**Supplemental Material**

Amaya\_etal\_model\_analog\_supplement\_revised\_notrac  
k.pdf